JOC The Journal of Organic Chemistry

pubs.acs.org/joc Article

Doubly Strapped Redox-Switchable 5,10,15,20-Tetraaryl-5,15-diazaporphyrinoids: Promising Platforms for the Evaluation of Paratropic and Diatropic Ring-Current Effects

Hikari Ochiai, Ko Furukawa, Haruyuki Nakano, and Yoshihiro Matano*

Cite This: J. Org. Chem. 2021, 86, 2283−2296 Read Online

ACCESS | Metrics & More | Article Recommendations | Supporting Information

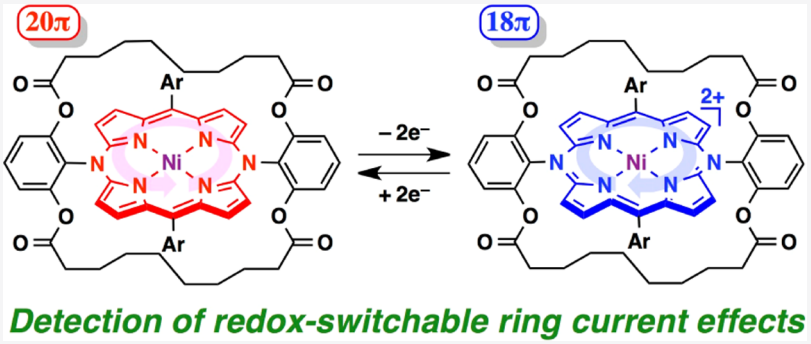

ABSTRACT: This paper presents a novel series of chemically stable and redox-switchable 20π, 19π, and 18π 5,10,15,20-tetraaryl-5,15-diazaporphyrinoids (TADAPs) that have two alkyl-chain straps above and below the diazaporphyrin ring. Three types of doubly strapped TADAPs were prepared as nickel(II) complexes using *meso*-*N*-(2,6-dihydroxyphenyl)-substituted TADAP and the corresponding aliphatic diacids as precursors. Theoretical calculations revealed that regardless of their oxidation states, all strapped TADAPs had essentially flat π-planes. It was found that the alkyl-chain straps slightly affected the optical and electrochemical properties of the DAP rings, particularly in the oxidized forms. ^{1}H NMR spectroscopy was used to evaluate the antiaromatic character of the 20π TADAPs and the aromatic character of the 18π TADAP dications, and it was observed that they displayed paratropic and diatropic ring-current effects, respectively, on the chemical shifts of methylene protons in the spatially separated alkyl chains. The degree of shielding and deshielding depended on the position of the methylene units; it decreased with increase in separation from the π-plane and central axis of the porphyrin ring. The NMR experiments also revealed that the degree of the diatropic ring currents was clearly related to the π-electron density of the porphyrin ring; the ring-current effects decreased as the charge increased from 0 to +2. These findings are also qualitatively supported by the nucleus-independent chemical shifts.

INTRODUCTION

Aromatic−antiaromatic switching of π-conjugated organic compounds has received considerable attention in the fields of structural and synthetic chemistry.[1−6] Porphyrins have been widely used as reliable platforms for identifying the aromaticity of (4n + 2)π and 4nπ macrocycles because their redox properties can be finely and systematically tuned either by chemical modification of the periphery or core-nitrogen atoms or by ring expansion.[7−12] In particular, significant attention has been dedicated toward the antiaromatic character of doubly reduced, 20π porphyrins.[10,11] The magnetic criteria of aromaticity are generally evaluated by NMR spectroscopy.[13] For example, Müllen et al. reported on the NMR spectra of potassium and lithium salts of 20π porphyrin dianions, wherein the peripheral pyrrolic-β and meso protons were observed at significantly higher fields than those of the 18π counterparts, with a difference of 9.9−10.4 ppm in the chemical shifts.[14] However, such anionic porphyrins are difficult to isolate and characterize under ambient conditions because of their extreme instability toward air and moisture. To overcome this limitation, several elaborate approaches, such as *N*-alkylation,[15−17] core modification,[18−20] peripheral functionalization,[21] and metal insertion,[22−24] have been developed to isolate 20π porphyrins in their neutral state. In many cases, however, the attachment of an excessive number of substituents causes the porphyrin ring to be severely distorted, thus impeding the experimental evaluation of the magnitudes of aromaticity and antiaromaticity associated with the 18π−20π redox processes. Therefore, the construction of a stable

Received: October 14, 2020
Published: January 7, 2021

https://dx.doi.org/10.1021/acs.joc.0c02433
J. Org. Chem. 2021, 86, 2283−2296

Scheme 1. Interconversion of TADAPs

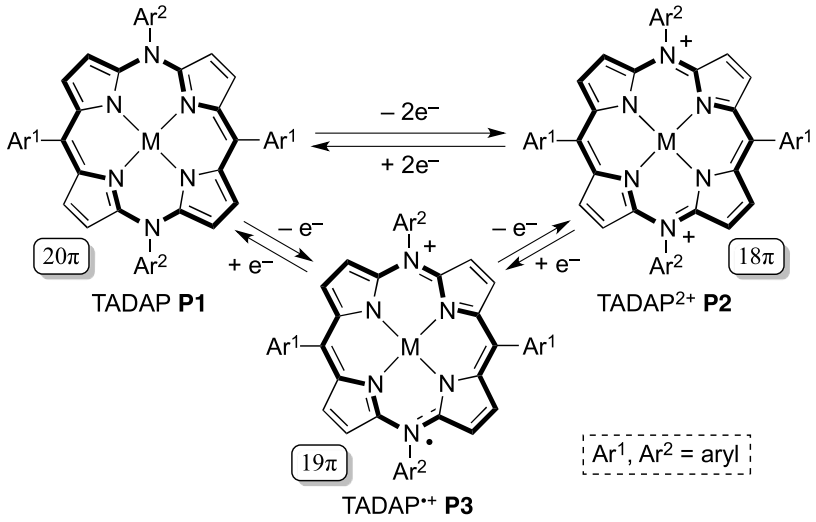

and flat porphyrin platform that is interconvertible between the 18π and 20π electron systems remains a challenge for the evaluation of porphyrin-induced paratropic and diatropic ring currents.

Partial replacement of the *meso* units of a porphyrin ring with nitrogen atoms lowers its molecular symmetry and stabilizes the highest occupied molecular orbital (HOMO) and lowest unoccupied molecular orbital (LUMO) of its π-electron system.[25−28] For example, the redox potentials of 5,15-diazaporphyrins (DAPs) differ substantially from those of their porphyrin counterparts.[28] Taking this into consideration, we recently reported on a new approach to stabilize 20π porphyrins by replacing two *meso* carbon atoms with two nitrogen atoms in 5,10,15,20-tetraarylporphyrin, thus altering the net charge of the porphyrin ring by two electrons.[29] Remarkably, several metal complexes and freebases of 5,10,15,20-tetraaryl-5,15-diazaporphyrinoids (TADAPs), namely, **P1**, **P2**, and **P3** (Scheme 1; M = Ni, Cu, Zn, 2H), were obtained as air-stable solids.[29−31] Most importantly, these TADAPs maintain highly flat π-planes and involve the same π-conjugation pathway, as described in Scheme 1. In this regard, **P1** is fairly different from the previously reported neutral 20π porphyrins that contain formal isophlorin frameworks passing through an outer 20π molecular perimeter.[32]

^{1}H NMR spectroscopy was used to evaluate the antiaromatic and aromatic characters of the reversibly redox-switchable TADAPs, **P1** and **P2**. It was observed that the chemical shifts of pyrrolic-β protons in **P1** and **P2** appeared at high and low fields, respectively, and the difference between these chemical shifts was approximately 4.0−5.0 ppm (for M = Ni). However, care should be taken when using chemical shifts of the peripheral protons as aromaticity indices because they are associated not only with the ring-current effects but also with the through-bond inductive/resonance effects. Presumably, the extent of the additional through-bond effects would be lower for the alkyl-chain straps located above and below a DAP ring. Thus, the quantification of the magnitude of aromaticity, based on the global ring-current effects arising from the 20π and 18π DAP rings, would be more precise if spatially separated alkyl chains are used as indicators.[33] On the basis of this presumption, we designed a series of novel TADAPs with alkyl-chain straps connected to the *meso*-*N*-aryl substituents via ester linkages. This paper presents the first examples of doubly strapped TADAPs and discusses their aromaticity.

RESULTS AND DISCUSSION

Synthesis. Scheme 2 illustrates the synthesis of oligomethylene-strapped TADAPs (C*n*-strapped TADAPs; *n* = 7, 8, 9) as nickel(II) complexes in the 20π (**7**), 19π (**8**), and 18π (**9**) forms. Metal-templated cyclization of bis[1-chloro-9-(2,6-dimethoxyphenyl)amino-5-mesityldipyrrin]−nickel(II) complex **1** (mesityl = 2,4,6-trimethylphenyl) was performed in the presence of K_2CO_3 in *N*,*N*-dimethylformamide (DMF) at 110 °C to produce 20π TADAP **2**. *O*-Demethylation of **2** with excess BBr_3 in CH_2Cl_2 afforded *meso*-*N*-2,6-dihydroxyphenyl derivative **3** with 19π electrons. *O*-Acylation of **3** with a mixture of excess acetic anhydride and pyridine afforded *meso*-*N*-2,6-diacetoxyphenyl derivative **4**, a 19π TADAP radical cation, which was then quantitatively converted to the 20π TADAP **5** and the 18π TADAP dication **6** by treatment with cobaltocene ($CoCp_2$) and $AgPF_6$, respectively. To increase its solubility, **3** was oxidized to the 18π structure with $AgPF_6$. Subsequently, it was condensed with 2 equiv of nonanedioic acid in the presence of *N*,*N*′-diisopropylcarbodiimide (DIC) and 4-dimethylaminopyridine (DMAP) in tetrahydrofuran (THF) to produce C7-strapped 20π TADAP **7-C7** that has two −OOC$(CH_2)_7$COO− bridges above and below the TADAP skeleton in 22% yield. Treatment of **7-C7** with $AgPF_6$ in CH_2Cl_2 yielded the 19π TADAP radical cation **8-C7**, which was further converted to the 18π TADAP dication **9-C7** by the sequential one-electron oxidation reaction with $AgPF_6$. C8-strapped and C9-strapped TADAPs (**7**/**8**/**9-C8** and **7**/**8**/**9-C9**, respectively) were prepared from **3** and the corresponding diacids by following a similar procedure (Scheme 2). All 18π TADAPs were reversibly converted to the corresponding 20π TADAPs by treatment with $CoCp_2$ (checked by UV−vis absorption spectroscopy). Both nonstrapped and strapped TADAPs were isolated as air-stable solids by column chromatography and/or recrystallization from the appropriate solvents.[34]

Scheme 3 illustrates the synthesis of the reference porphyrins. The nickel(II) complex of 5,15-bis(2,6-dihydroxyphenyl)-10,20-dimesitylporphyrin **11** was prepared by the metallation of freebase **10**[35] with $Ni(OAc)_2{\cdot}4H_2O$. Non-

https://dx.doi.org/10.1021/acs.joc.0c02433
J. Org. Chem. 2021, 86, 2283−2296

Scheme 2. Synthesis of Strapped TADAPs

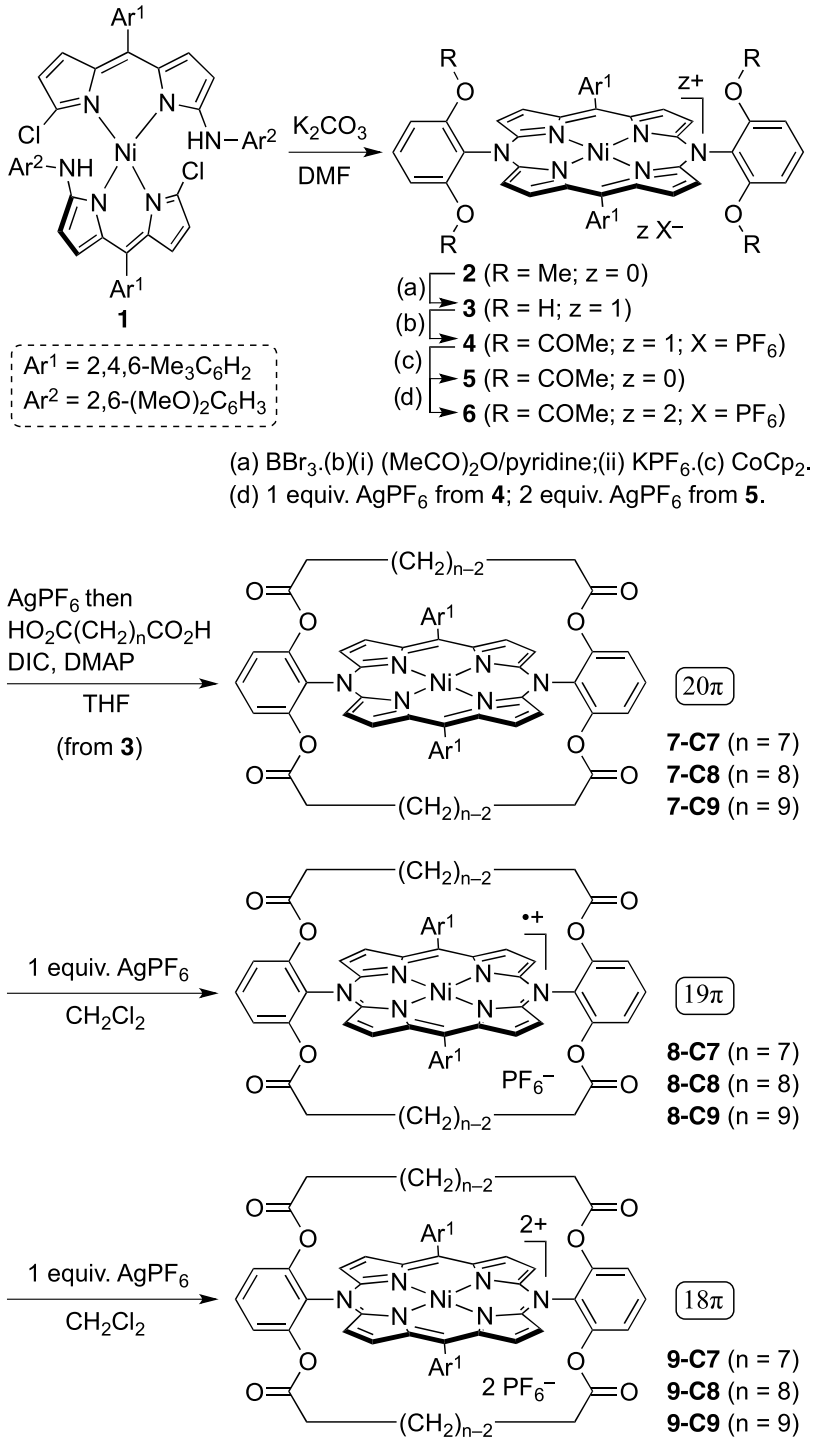

strapped 18π porphyrin **12** and strapped 18π porphyrins **13-C*n*** (n = 7, 8, 9) were obtained by the acylation of **11** with acetic anhydride and the corresponding diacid dichlorides, respectively. Diphenyl diesters **14-C*n*** (n = 7, 8, 9; Figure 4) were also prepared as references from the corresponding aliphatic diacid chlorides and phenol (see the Experimental Section).

Structures. The structures of the novel TADAPs and the reference compounds were characterized by NMR and IR spectroscopies and high-resolution electrospray ionization (ESI) mass spectrometry. The ESI mass spectra revealed that the base peaks corresponded to either the molecular ions (for **7-C*n***) or the fragment cations (for **8-C*n*** and **9-C*n***). The IR spectra displayed the peaks corresponding to the C═O stretching bands of **7-C*n***, **9-C*n***, and **13-C*n*** at higher frequencies (1758−1770 cm^{-1}) than those of **14-C*n*** (1745−1749 cm^{-1}). X-ray crystallography was used to elucidate the crystal structures of **7-C8** and **7-C9** although the quality of their crystallographic data is not at a publishable level.[36] The currently available data (not reported herein) revealed the following structural features. (i) Both **7-C8** and **7-C9** have flat DAP π-planes, as observed for the previously reported 20π

https://dx.doi.org/10.1021/acs.joc.0c02433
J. Org. Chem. 2021, 86, 2283−2296

Scheme 3. Synthesis of Strapped Porphyrins

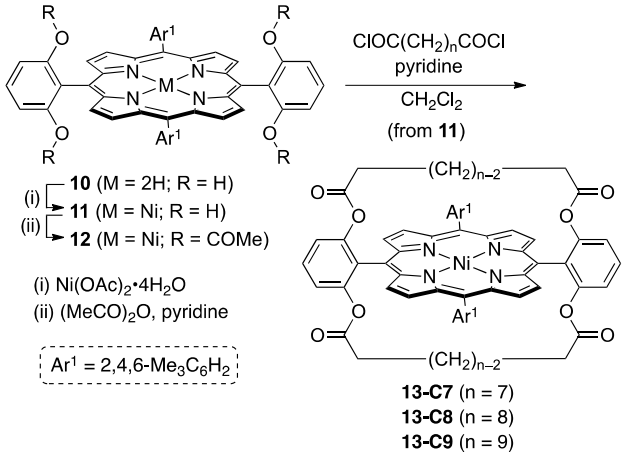

TADAP **P1** (M = Ni; 5,15-Ar = *p*-*t*BuC_6H_4; 10,20-Ar = mesityl).[28] (ii) The *meso*-aryl rings are almost perpendicular to the DAP ring, suggesting that there is an insignificant amount of π-conjugative interaction between the *meso*-aryl groups and the DAP ring. (iii) The O−C═O units of the *ortho*-ester groups are twisted away from the adjacent benzene rings. (iv) The bridging alkyl chains have essentially *anti*- or *gauche*-staggered conformation.

To further examine the structures of TADAPs **5**−**9** and porphyrins **12** and **13**, density functional theory (DFT) calculations were performed at the B3LYP/6−311G(d,p) level of theory. The structural parameters of **7-C8** and **7-C9** obtained by X-ray crystallographic analysis were used for setting their initial structures. The optimized structures of **7-C8** and **7-C9** were further used as models for examining the C8- and C9-strapped derivatives. The structures of the C7-strapped and nonstrapped derivatives were optimized by various global symmetries (C_i, C_2, and C_1). Although several metastable structures with small differences in energy (<1 kcal mol^{-1}) were predicted by DFT calculations, the bond parameters of their porphyrin rings were almost identical to each other. The optimized structures of **7-C*n*** with their point groups are presented in Figure 1, and all of the structures, along with some selected orbital diagrams, are shown in Figures S1−S4 in the Supporting Information (SI). The bond lengths, bond angles, and torsion angles are summarized in Tables S1 and S2 in the SI.

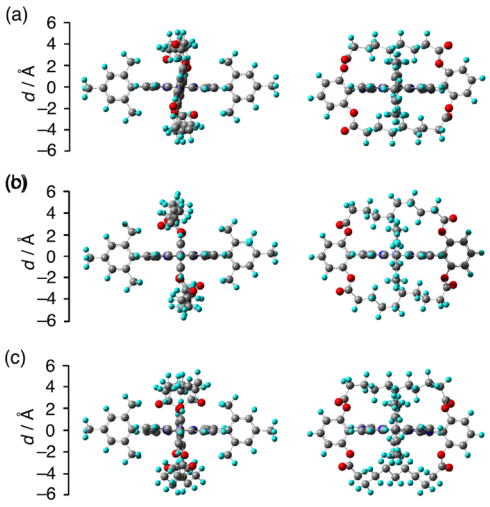

Figure 1. Optimized structures of (a) **7-C7** (C_i), (b) **7-C8** (C_i), and (c) **7-C9** (C_1) calculated by the DFT method. Front views (left) and side views (right).

The structural information obtained by the DFT calculations is as follows. (i) Regardless of the oxidation state, alkyl-chain length, and molecular symmetry, the DAP rings in the strapped derivatives are essentially flat. (ii) The in-plane C−C/C−N bond lengths and C−N_{meso}−C/C−C$_{meso}$−C bond angles of **7-C*n***, **9-C*n***, and **13-C*n*** are in good accordance with those of **5**, **6**, and **12**, respectively. (iii) In the bridging alkyl chains, the two adjacent methylene units adopt *anti*- or *gauche*-staggered conformation. (iv) The carbonyl groups of the *ortho*-ester linkages are twisted to maintain the staggered conformation of the alkyl chains. This result is consistent with the previously mentioned IR observations as the distortion of the *ortho*-ester moieties may weaken the resonance interactions between the carbonyl and phenoxy groups. (v) The *meso*-mesityl rings are perpendicular to the DAP/porphyrin rings, whereas the *meso*-2,6-diacyloxyphenyl groups in **6** and the C7-strapped derivatives are inclined toward the rings. The C7-strapped derivatives show the most significant inclination in each oxidation state. (vi) Depending on the oxidation states and charges of the porphyrin rings, the positions of the methylene units differ slightly in **7-C*n***, **9-C*n***, and **13-C*n***, possessing the same alkyl-chain straps (Table S2 and Figure S5 in the SI). These structural features are significantly related to the magnitude of ring-current effects caused by the DAP/porphyrin rings (vide infra).

Optical and Electrochemical Properties. The optical and electrochemical properties of the TADAPs and the reference porphyrins were investigated by ultraviolet/visible/near-infrared (UV−vis−NIR) absorption spectroscopy (Figure 2) and cyclic voltammetry (Figure 3), and the data are summarized in Table 1. The UV−vis−NIR spectra of the strapped TADAPs **7-C*n***, **8-C*n***, and **9-C*n*** were similar to those of the nonstrapped TADAPs **5**, **4**, and **6**, respectively. The 20π TADAPs **7-C*n*** exhibited two intense absorption bands with the absorption maxima (λ_{max}) of 443−444 and 522−523 nm, whereas the 18π dications **9-C*n*** exhibited two intense bands with λ_{max} of 394−397 and 631−651 nm. The Q-like bands of **9-C*n*** were red-shifted by 1670−2100 cm^{-1} relative to the corresponding Q bands of **13-C*n*** (λ_{max} = 558 nm), indicating that the optical HOMO−LUMO gaps of the 18π TADAP dications were substantially smaller than those of the isoelectronic porphyrins. The main characteristics of the π−π* electronic excitations in the 20π, 19π, and 18π TADAPs were previously assigned by the time-dependent DFT calculations.[30] The lowest-energy absorption bands of **8-C7** (SOMO−1-to-SOMO excitation; SOMO: singly occupied molecular orbital) and **9-C7** (HOMO-to-LUMO excitation) are slightly broader and red-shifted compared with those of **8-C8**/**8-C9** and **9-C8**/**9-C9**, respectively. Electrochemical data, discussed in the following section, suggest that shorter alkyl chains may perturb the orbital energies of the cationic DAP rings, indicating that the excitation energies and spectral shapes of the strapped TADAP cations are influenced by the alkyl-chain lengths.

Redox potentials of **2**, **4**, **7-C*n***, **12**, and **13-C*n*** were measured in CH_2Cl_2 by cyclic voltammetry using Bu_4NPF_6 as the supporting electrolyte. As shown in Figure 3, TADAPs **4** and **7-C*n*** displayed two reversible redox processes with a difference in potentials of 0.64−0.87 V. The 20π/19π half-

https://dx.doi.org/10.1021/acs.joc.0c02433
J. Org. Chem. 2021, 86, 2283−2296

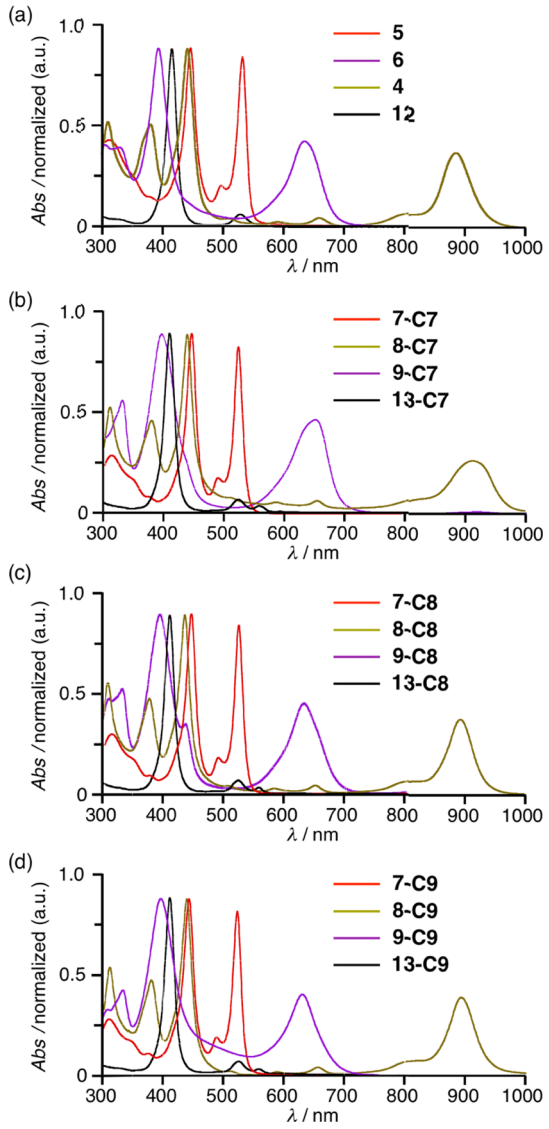

Figure 2. Normalized UV−vis−NIR absorption spectra of (a) **4**, **5**, **6**, and **12**, (b) **7-C7**, **8-C7**, **9-C7**, **13-C7**, (c) **7-C8**, **8-C8**, **9-C8**, **13-C8**, and (d) **7-C9**, **8-C9**, **9-C9**, **13-C9** in CH_2Cl_2.

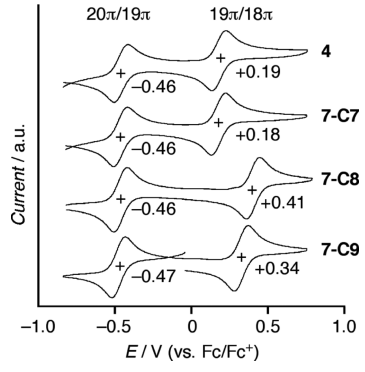

Figure 3. Cyclic voltammograms of **4**, **7-C7**, **7-C8**, and **7-C9**. Measured in CH_2Cl_2 with Bu_4NPF_6 as a supporting electrolyte. Scan rate was 60 mV s^{-1}.

wave potentials of **4**, **7-C7**, **7-C8**, and **7-C9** were almost identical to each other ($E_{1/2}$ = −0.46 to −0.47 V vs ferrocene/ferrocenium; Fc/Fc^+), indicating that the alkyl-chain straps have a negligible impact on the energies of the HOMO in their 20π DAP rings. However, it was observed that the 19π/18π half-wave potentials differ from each other; the substantial reduction potential of **9-C7** ($E_{1/2}$ = +0.18 V) is similar to that of **4** ($E_{1/2}$ = +0.19 V), but those potentials are negatively shifted compared with those of **9-C8** ($E_{1/2}$ = +0.41 V) and **9-C9** ($E_{1/2}$ = +0.34 V). These findings suggest that the energy levels of the LUMOs in **9-C*n*** are sensitive toward the alkyl-chain length although the reason behind this has not been clearly understood. In contrast, the influence of the alkyl-chain length on the 18π/17π redox processes of porphyrins **12** and **13-C*n*** is almost insignificant ($E_{1/2}$ = +0.60 to +0.63 V vs Fc/Fc^+).

Table 1. Optical and Electrochemical Data for TADAPs and Porphyrins[a]

compd	λ_{max}/nm[b] (log ε)	E/V[c]
2	445 (5.01), 531 (4.99)	−0.68, +0.08
4	380 (4.72), 439 (4.97), 903 (4.54)	−0.46, +0.19
5	448 (n.d.), 535 (n.d.)	n.d.
6	392 (4.81), 627 (4.51)	n.d.
7-C7	444 (5.00), 522 (4.97)	−0.46, +0.18
7-C8	444 (5.14), 522 (4.95)	−0.46, +0.41
7-C9	443 (4.96), 523 (4.94)	−0.47, +0.34
8-C7	380 (4.61), 439 (4.90), 914 (4.37)	n.d.
8-C8	379 (4.61), 438 (4.88), 895 (4.50)	n.d.
8-C9	379 (4.60), 438 (4.87), 894 (4.52)	n.d.
9-C7	397 (n.d.), 651 (n.d.)	n.d.
9-C8	394 (n.d.), 634 (n.d.)	n.d.
9-C9	397 (n.d.), 631 (n.d.)	n.d.
12	412 (5.57), 527 (4.43), 559 (4.05)	+0.60, +0.82[d]
13-C7	410 (5.55), 524 (4.42), 558 (4.12)	+0.62[d,e]
13-C8	411 (5.51), 524 (4.40), 558 (4.08)	+0.63[d,e]
13-C9	411 (5.61), 524 (4.45), 558 (4.01)	+0.60[d,e]

[a]Measured in CH_2Cl_2. n.d., not determined. [b]The values of λ_{max} > 350 nm and log ε > 4 are listed. [c]Half-wave potentials (vs Fc/Fc^+) measured by cyclic voltammetry with Bu_4NPF_6 as the electrolyte. [d]The oxidation processes are listed. [e]The quasi-reversible or irreversible oxidation peaks were observed at E_{pa} = ca. +1.2−1.35 V vs Fc/Fc^+.

Antiaromaticity and Aromaticity. TADAPs **7-C*n*** and **9-C*n*** are the ideal candidates for identifying antiaromatic and aromatic characters of the 20π and 18π porphyrinoids, respectively, as the two unshared electron pairs on their *meso*-nitrogen atoms are involved in their π-networks. As mentioned earlier, precise information regarding the ring currents above and below the DAP π-planes can be obtained by analyzing the chemical shifts of the methylene protons in the bridging alkyl chains of **7**/**9**. The assignment of the CH_2 signals was verified by $^1H-^1H$ COSY. The structures and numbering of the CH_2 units of TADAPs **7**/**9**, porphyrins **13**, and the reference diesters **14** are illustrated in Figure 4. The ^1H NMR spectra of the C8-strapped derivatives are shown in Figure 5, and those of the C7- and C9-strapped derivatives are shown in Figures S6 and S7, respectively, in the SI. On an average, **7**, **9**, and **13** have symmetric structures, as indicated by their NMR spectra. They exhibited four (for **7**/**9**/**13-C7** and **7**/**9**/**13-C8**) or five (for **7**/**9**/**13-C9**) signals corresponding to the bridging methylene protons and two signals corresponding to the pyrrolic-β protons, implying that the conformational changes of their alkyl chains are rapid on the NMR time scale. The chemical shifts (δ) of the bridging methylene and pyrrolic-

https://dx.doi.org/10.1021/acs.joc.0c02433
J. Org. Chem. 2021, 86, 2283−2296

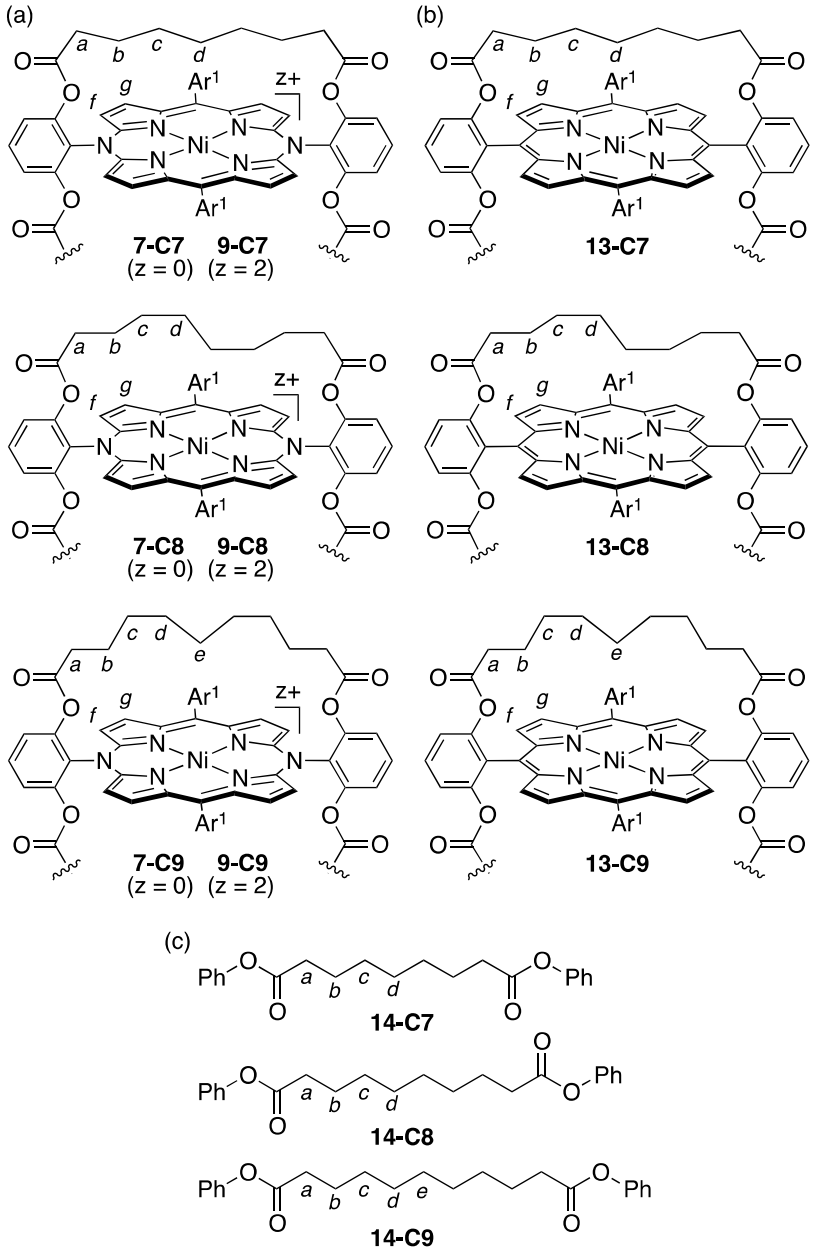

Figure 4. Partial structures of (a) **7**, **8**, and **9** (z denotes the charge number) and (b) **13**. Ar^1 = mesityl. (c) Structures of **14**.

β protons are detailed in Table S4 in the SI. The signals of the pyrrolic-β protons (f and g) of **7-C*n*** appeared at 3.59−3.61 and 4.50−4.52 ppm, whereas those of **9-C*n*** appeared at 8.77−8.86 and 8.58−8.69 ppm, respectively. The high-field and low-field appearances of these peripheral protons confirm the paratropic (20π) and diatropic (18π) ring-current effects in **7** and **9**, respectively. The differences between the chemical shifts ($\Delta\delta$) of the methylene-proton signals (a−e) of TADAPs/porphyrins (**7-C*n***, **9-C*n***, and **13-C*n***) and those of the corresponding reference diesters **14-C*n*** are plotted in Figure 6. As expected, the $\Delta\delta$ values are mainly related to the global paratropic and diatropic ring-current effects. An analysis of the plot reveals the following information. (i) The absolute $\Delta\delta$ values observed for the C8- and C9-strapped derivatives increase in the order $a < b < c < d$ ($<e$), indicating that the inner methylene protons experience stronger shielding/deshielding effects arising from the ring currents. (ii) The absolute $\Delta\delta$ values of the C7-strapped TADAPs show irregular orders, $a < c < b < d$ for **7-C7** and $a < c < d < b$ for **9-C7**. These results may reflect the low flexibility of the bridging C7-alkyl chains. (iii) The absolute $\Delta\delta$ values of the central methylene units of the C7-strapped derivatives (d) are larger than those of the C9-strapped derivatives (e) for all three π-electron systems. (iv) For most methylene protons, the absolute $\Delta\delta$ values of the TADAP dications **9-C*n*** are smaller than those of the corresponding porphyrin counterparts **13-C*n***, thus reflecting the difference in the net charge between these two 18π-electron systems.

To further investigate the ring-current effects, the nucleus-independent chemical shifts (NICS)[37−41] were evaluated at 73 × 73 lattice positions (from −3.6 to +3.6 Å for x- and y-axes with a pitch of 0.1 Å and from 1 to 5 Å for the z-axis with a pitch of 1 Å) above the π-planes of the zinc(II) complexes of 5,15-dihydro-5,15-diazaporphyrinoids (DHDAP) **15** (20π) and **16** (18π dication) and the 18π porphine **17**. These compounds were selected to exclude the excessive electronic

https://dx.doi.org/10.1021/acs.joc.0c02433
J. Org. Chem. 2021, 86, 2283−2296

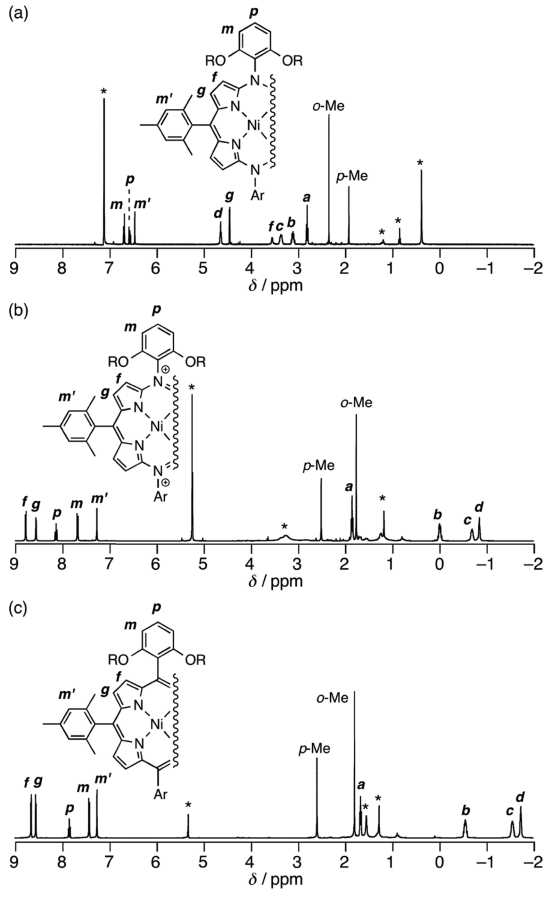

Figure 5. ^{1}H NMR spectra of (a) **7-C8** in C_6D_6, (b) **9-C8** in CD_2Cl_2, and (c) **13-C8** in CD_2Cl_2. Asterisks indicate residual solvent peaks. Assignments of *a*–*d* are indicated in Figure 4.

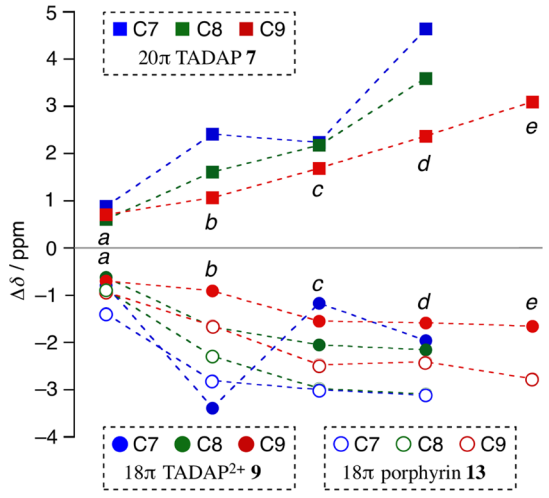

Figure 6. Differences in ^{1}H NMR chemical shifts ($\Delta\delta$) of the bridging CH_2 protons of **7**, **9**, and **13** vs **14**. For the numbering of the CH_2 groups (*a*–*e*), see Figure 4.

effects caused by a nickel atom from the NICS calculations. The isotropic NICS(n) and their out-of-plane components, NICS(n)zz, are plotted as contour maps in Figure S8 in the SI and Figure 7, respectively. The NICS-scan method reported herein was found to be significantly more coherent than the evaluation using a single NICS value for identifying diamagnetic and paramagnetic ring currents of aromatic and antiaromatic molecules, respectively.[42,43] The NICS(n)zz maps provided the following information on the ring-current effects observed in **7**, **9**, and **13**. (1) The absolute NICS(n)zz values of **15**, **16**, and **17** gradually decrease with an increase in the vertical distance from the π plane and horizontal distance from the central axis, thus qualitatively supporting the experimental results. (2) The contour maps of **15** indicate that the global paratropic ring currents are dominant around the central axis at heights of 2–5 Å, where some bridging methylene protons may be present. For **15**, the local diatropic ring currents are merged above the four pyrrole rings. (3) The absolute NICS(n)zz values of **16** are considerably smaller than those of **17** at each height (n = 1–5), suggesting that the neutral porphyrin ring in **13** exhibits larger diatropic ring-current effects on the bridging alkyl chains than those of the cationic TADAP ring in **9**. This explicitly reflects a difference in the π-electron density between **17** (**13**) and **16** (**9**).[44,45] (4) The irregular orders observed for **7-C7** and **9-C7** (Figure 6) are noteworthy. The absolute $\Delta\delta$ values of CH_2-*b* for these C7-strapped derivatives are considerably larger than those of the others, suggesting that the CH_2-*b* units retain their average positions near the DAP rings (Figure S5 in the SI). This is probably because the relatively short alkyl chains cause them to be less flexible. Thus, it can be concluded that the alkyl-chain straps can be used as promising indicators for the experimental identification of the paratropic and diatropic ring currents arising from the 20π- and 18π-electron systems, respectively, in DAP/porphyrin rings.

EPR and NMR spectra of 19π TADAPs. Electron paramagnetic resonance (EPR) spectroscopy revealed that an unshared electron spin of TADAP radical cation **8** was completely delocalized over the DAP ring (Figure S9 in the SI). The *g* values and the hyperfine coupling (*hfc*) constants of **8-C8** are very similar to those of **4**, and the calculated spin distribution of **8-C8** supports the observed fine structure. The *g* and *hfc* values of **8-C7** and **8-C9** are almost identical to those of **8-C8**. These results indicate that the alkyl-chain straps have little influence on the delocalization of the unshared electron spin of the strapped 19π TADAP radical.

In general, NMR spectroscopy is not used for evaluating the ring-current effects of porphyrin π-radicals because a strong nuclear–electron spin–spin coupling occurs, which induces fast electronic relaxations and causes significant line-broadening of the peripheral proton peaks.[46] This behavior was observed for **P3**, which did not show any detectable NMR signals for the pyrrolic-β protons. In contrast, the ^{1}H NMR spectra of **8-C*n*** exhibited broadened signals in the range of 1–2.6 ppm due to the bridging methylene protons (Figure 8). Other than these, no assignable ^{1}H NMR signals were detected. Therefore, it is likely that compared with the pyrrolic-β and *meso*-aryl protons, the spatially separated alkyl-strap methylene protons of **8-C*n*** experience a considerably weaker ring-current effect due to the electron–nucleus spin–spin interactions. It is apparent that the 19π DAP rings in **8-C*n*** produce negligible ring currents, and thus, they do not alter the chemical shifts of the bridging methylene protons. These findings demonstrate that the strapped TADAPs can also be used as probes to experimentally evaluate the ring-current effects caused by porphyrin-based 19π-electron systems.

■ CONCLUSIONS

Doubly strapped TADAPs in the three different oxidation states, 18π, 19π, and 20π, were successfully designed and

https://dx.doi.org/10.1021/acs.joc.0c02433
J. Org. Chem. 2021, 86, 2283–2296

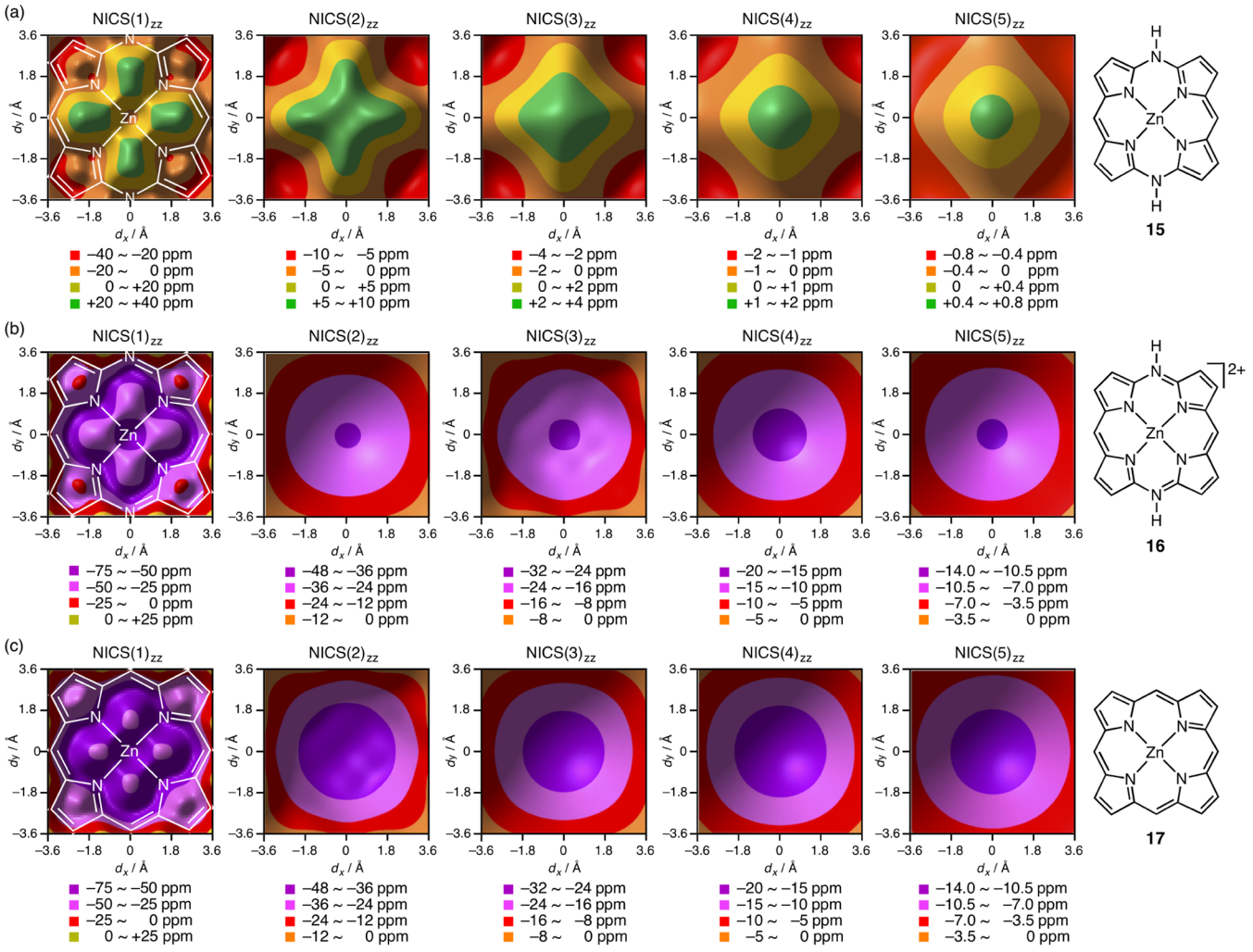

Figure 7. Contour maps of the NICS(n)zz values (n = 1, 2, 3, 4, 5) at the 73 × 73 lattice positions (lattice pitch = 0.1 Å for x- and y-axes; the zinc center is placed at $x = y = 0$) calculated by the Hartree−Fock method: (a) **15** (D_{2h}), (b) **16** (D_{2h}), and (c) **17** (D_{4h}).

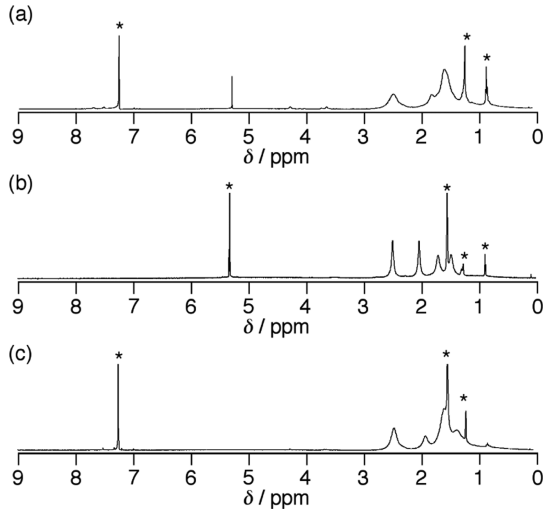

Figure 8. ^{1}H NMR spectra of (a) **8-C7** in $CDCl_3$, (b) **8-C8** in CD_2Cl_2, and (c) **8-C9** in $CDCl_3$. Asterisks indicate residual solvent peaks.

synthesized as platforms for the identification of the ring currents arising from these porphyrinoids. In addition, reference compounds, nonstrapped TADAPs, and similarly strapped 18π porphyrins were prepared. The DFT calculations, as well as the preliminary X-ray crystallographic analyses, revealed that regardless of the oxidation states, all strapped TADAPs possess flat π-planes. The bridging alkyl chains adopt staggered conformations, and depending on the number of the methylene units, these chains occupy different spaces above and below the porphyrin π-plane. The flexibility of the straps may be somewhat restricted in the cationic TADAPs with short alkyl-chain straps. NMR spectroscopy of the strapped TADAPs clearly confirmed the antiaromatic and aromatic characters of 20π and 18π TADAPs, respectively. Both the paratropic and diatropic ring-current effects were experimentally evaluated based on the differences in chemical shifts ($\Delta\delta$) of the bridging methylene protons, which show an insignificant amount of through-bond electronic effects. The observed $\Delta\delta$ values implied that the ring-current effects decreased with increase in separation from the porphyrin π-plane and central axis of the porphyrin ring. This was in accordance with the NICS(n)zz values calculated for their bare models, 20π and 18π 5,15-dihydro-5,15-diazaporphyrinoids and 18π porphine. It is also noteworthy that the charge, i.e., the π-electron densities of the 18π porphyrin rings, impacted the ring currents; the TADAP dications generated weaker diatropic ring currents than those generated by the porphyrin counter-

https://dx.doi.org/10.1021/acs.joc.0c02433
J. Org. Chem. 2021, 86, 2283−2296

parts. This paper provides detailed experimental information on the ring-current effects arising from flat 20π and 18π porphyrins, which have the same π-conjugation pathway. Further studies on the development of three-dimensionally functionalized diazaporphyrinoids are being conducted.

EXPERIMENTAL SECTION

General Remarks. All melting points were recorded on a micro melting point apparatus and are uncorrected. NMR spectra were recorded on 700 MHz and/or 400 MHz spectrometers. The ^{1}H and ^{13}C chemical shifts are reported in ppm as relative values vs tetramethylsilane (in $CDCl_3$ and CD_2Cl_2) or a solvent residual signal (δ_H 7.16 ppm in C_6D_6), and the ^{31}P chemical shifts are reported in ppm vs H_3PO_4. High-resolution mass spectra (HRMS) were measured using an electron spray ionization (ESI)−quadrupole method. UV−vis−NIR absorption spectra were recorded in the range of 300−1000 nm. For some compounds, the relative intensities are reported instead of molar extinction coefficients because a trace amount of oxidized/reduced species was generated during the measurement of sample solutions. IR spectra were obtained using an attenuated total reflection (ATR) method. Electrochemical measurements were performed using a glassy carbon working electrode, a platinum wire counter electrode, and a Ag/Ag^+ [0.01 M $AgNO_3$, 0.1 M Bu_4NPF_6 (MeCN)] reference electrode. Chemicals and solvents were of reagent grade quality and used without further purification unless otherwise noted. Thin-layer chromatography and preparative column chromatography were performed using silica gel (neutral). All reactions were performed under an argon or nitrogen atmosphere unless otherwise noted.

Synthesis and Characterization of New Compounds. *Synthesis of* ***1****.* (i) A mixture of 1,9-dichloro-5-mesityldipyrromethene (908 mg, 2.74 mmol), 2,6-dimethoxyaniline (1.01 g, 6.58 mmol), and MeCN (30 mL) was stirred for 19 h at room temperature. After being quenched with water, the aqueous layer was extracted with CH_2Cl_2, and the combined organic extracts were dried over Na_2SO_4 and evaporated under reduced pressure. The residue was subjected to silica-gel column chromatography (hexane/AcOEt = 5/1). The fraction of R_f = 0.4 (hexane/AcOEt = 5/1) was collected and evaporated to give 1-chloro-9-(2,6-dimethoxyphenyl)amino-5-mesityldipyrromethene **18** (the structure is shown in Figure S10 in the SI) as a red solid (1.267 g, 100%). Mp 82−84 °C. ^{1}H NMR ($CDCl_3$, 400 MHz): δ 7.18 (d, 1H, J = 8.4 Hz), 6.89 (s, 2H), 6.68 (d, 2H, J = 8.4 Hz), 6.58 (s, 1H), 6.44 (d, 1H, J = 4.6 Hz), 6.04 (d, 1H, J = 4.6 Hz), 5.95 (d, 1H, J = 4.0 Hz), 5.83 (d, 1H, J = 4.0 Hz), 3.91 (s, 6H), 2.33 (s, 3H), 2.10 (s, 6H). The pyrrolic NH proton was not clearly observed. ^{13}C{^{1}H} NMR ($CDCl_3$, 100 MHz): δ 163.1, 153.8, 144.3, 137.6, 136.9, 134.2, 133.3, 133.0, 128.7, 127.7, 125.9, 123.1, 117.2, 117.1, 116.4, 109.1, 104.3, 55.9, 21.1, 20.0. HRMS (ESI) m/z: $[M + H]^+$ calcd for $C_{26}H_{27}ClN_3O_2$ 448.1792; found 448.1774. (ii) A mixture of **18** (392 mg, 1.18 mmol), $Ni(OAc)_2{\cdot}4H_2O$ (110 mg, 0.444 mmol), MeOH (10 mL), and CH_2Cl_2 (10 mL) was stirred for 16 h at room temperature. The mixture was concentrated under reduced pressure to leave a solid residue, which was reprecipitated from MeOH to give **1** as a gray solid (360 mg, 86%). R_f = 0.4 (hexane/AcOEt = 5/1). Mp 168−170 °C. HRMS (ESI): m/z $[M]^+$ calcd for $C_{52}H_{50}Cl_2N_6NiO_4$ 950.2619; found 950.2634. The ^{1}H and ^{13}C NMR data/spectra of **1** are not reported because of its paramagnetic character.

Synthesis of ***2****.* A mixture of **1** (351 mg, 0.368 mmol), K_2CO_3 (1.05 g, 7.57 mmol), and DMF (20 mL) was stirred for 31 h at 110 °C. After being quenched with water, the aqueous layer was extracted with toluene, and the combined organic extracts were washed with brine, dried over Na_2SO_4, and evaporated under reduced pressure. The residue was reprecipitated from CH_2Cl_2−MeOH to give **2** as a reddish-brown solid (245 mg, 76%). R_f = 0.3 (hexane/AcOEt = 5/1). Mp > 300 °C. ^{1}H NMR (C_6D_6, 400 MHz): δ 6.78 (t, 2H, J = 8.4 Hz), 6.52 (s, 4H), 6.04 (d, 4H, J = 8.4 Hz), 4.85 (d, 4H, J = 4.4 Hz), 3.78 (d, 4H, J = 4.4 Hz), 3.30 (s, 12H), 2.34 (s, 12H), 1.93 (s, 6H). ^{13}C{^{1}H} NMR (C_6D_6, 100 MHz): δ 160.8, 158.0, 140.5, 137.0, 136.5, 136.2, 133.3, 129.7, 127.2, 116.6, 104.8, 102.1, 79.7, 55.6, 21.0, 19.4. HRMS (ESI) m/z: $[M]^+$ calcd for $C_{52}H_{48}N_6NiO_4$ 878.3091; found 878.3093. UV−vis (CH_2Cl_2): λ_{max} (log ε) 445 (5.01), 531 nm (4.99).

Synthesis of ***3****.* To a solution of **2** (193 mg, 0.220 mmol) in CH_2Cl_2 was added BBr_3 (7.6 mL, 7.6 mmol), and the mixture was stirred for 16 h at room temperature. After being quenched with water, the aqueous layer was extracted with CH_2Cl_2, and the combined organic extracts were washed with an aqueous $NaHCO_3$ solution, dried over Na_2SO_4, and evaporated under reduced pressure. The residue was then reprecipitated from MeOH−Et_2O to give crude **3** as a green solid (190 mg). Although we did not characterize the counteranion of **3**, bromide or bicarbonate is plausible. In the following experiments, the molar quantity of **3** was calculated assuming that the counteranion is bromide. Compound **3** was kept as a solid until the following condensation reactions; HRMS (ESI) m/z: $[M - X]^+$ calcd for $C_{48}H_{40}N_6NiO_4$ 822.2459; found 822.2457. UV−vis−NIR (CH_2Cl_2): λ_{max} (relative intensity) 388 (1), 443 (0.90), 880 nm (0.30). The ^{1}H and ^{13}C NMR data/spectra of **3** are not reported because of its paramagnetic character.

Synthesis of ***4****.* A mixture of **3** (31 mg, ca. 0.034 mmol), acetic anhydride (0.10 mL, 1.1 mmol), pyridine (50 μL, 0.96 mmol), and CH_2Cl_2 (15 mL) was stirred at room temperature. After 27 h, an aqueous 1 M HCl solution was added, and the separated organic phase was washed with an aqueous $NaHCO_3$ solution. To the washed organic phase was added an aqueous KPF_6 solution, and the resulting mixture was vigorously stirred for 20 min. The organic phase was separated, dried over Na_2SO_4, and evaporated under reduced pressure. The residue was subjected to silica-gel column chromatography (CH_2Cl_2/MeOH = 40/1). The fraction of R_f = 0.4 (CH_2Cl_2/MeOH = 20/1) was collected and evaporated to leave a solid residue, which was reprecipitated from hexane−CH_2Cl_2 to give **4** as a gray solid (20 mg, 48%). Mp > 300 °C. ^{31}P{^{1}H} NMR ($CDCl_3$, 162 MHz): δ −143.7 (septet, J_{P-F} = 716.2 Hz). HRMS (ESI) m/z: $[M - PF_6]^+$ calcd for $C_{56}H_{48}N_6NiO_8$ 990.2882; found 990.2879. IR (ATR): ν 1778 (C═O), 838 (P−F) cm^{-1}. UV−vis−NIR (CH_2Cl_2): λ_{max} (log ε) 380 (4.72), 439 (4.97), 903 nm (4.54). The ^{1}H and ^{13}C NMR data/spectra of **4** are not reported because of its paramagnetic character.

Synthesis of ***5****.* A mixture of **4** (6.7 mg, 5.3 μmol), cobaltocene (1.0 mg, 5.4 μmol), and toluene (3 mL) in a 50 mL flask was sonicated for 5 min at room temperature. The resulting mixture was filtered through a thin silica-gel bed, and the filtrate was concentrated under reduced pressure. The solid residue was reprecipitated from hexane to give **5** as an orange solid (4.5 mg, 86%). Mp > 300 °C. ^{1}H NMR (C_6D_6, 400 MHz): δ 6.80 (d, 4H, J = 8.3 Hz), 6.65 (t, 2H, J = 8.3 Hz), 6.52 (s, 4H), 4.77 (d, 4H, J = 4.4 Hz), 3.86 (d, 4H, J = 4.4 Hz), 2.43 (s, 12H), 2.30 (s, 12H), 1.99 (s, 6H). Prolonged standing of **5** in solution caused the generation of a small amount of the 19π radical, which hampered in obtaining the high-quality ^{13}C NMR spectrum of **5**. HRMS (ESI) m/z: $[M]^+$ calcd for $C_{56}H_{48}N_6NiO_8$ 990.2887; found 990.2887. IR (ATR): ν 1769 (C═O) cm^{-1}. UV−vis (CH_2Cl_2): λ_{max} (relative intensity) 448 (1), 535 nm (0.79).

Synthesis of ***6****.* A mixture of **4** (4.8 mg, 4.2 μmol), $AgPF_6$ (1.0 mg, 4.0 μmol), and CH_2Cl_2 (10 mL) was stirred for 5 min at room temperature. The resulting mixture was filtered through a thin silica-gel bed, and the filtrate was concentrated under reduced pressure. The solid residue was reprecipitated from hexane to give **6** as a green solid (4.2 mg, 78%). Mp > 300 °C. ^{1}H NMR (CD_2Cl_2, 400 MHz): δ 8.67 (d, 4H, J = 5.2 Hz), 8.39 (d, 4H, J = 5.2 Hz), 8.11 (t, 2H, J = 8.4 Hz), 7.67 (d, 4H, J = 8.4 Hz), 7.28 (s, 4H), 2.56 (s, 6H), 1.87 (s, 12H), 1.49 (s, 12H). Prolonged standing of **6** in solution caused the generation of a small amount of the 19π radical, which hampered in obtaining the high-quality ^{13}C NMR spectrum of **5**. HRMS (ESI) m/z: $[M - 2\ PF_6]^{2+}$ calcd for $C_{56}H_{48}N_6NiO_8$ 990.2882 (z = 1), 495.1438 (z = 2); found 990.2882 (z = 1), 495.1437 (z = 2). IR (ATR): ν 1777 (C═O), 834 (P−F) cm^{-1}. UV−vis (CH_2Cl_2): λ_{max} (log ε) 392 (4.81), 627 nm (4.51).

Synthesis of ***7****.* Typical procedure: To a CH_2Cl_2 solution of **3** (16.7 mg, ca. 0.019 mmol) was added $AgPF_6$ (3.8 mg, 0.015 mmol), and the resulting solution was filtered through a thin Celite bed. The

https://dx.doi.org/10.1021/acs.joc.0c02433
J. Org. Chem. 2021, 86, 2283−2296

formation of an 18π species was confirmed by HRMS spectrometry [m/z [M − 2 PF_6]$^{z+}$ calcd for $C_{48}H_{40}N_6NiO_4$ 822.2459 (z = 1), 411.1227 (z = 2); found 822.2457 (z = 1), 411.1227 (z = 2)] and UV−vis absorption spectroscopy (λ_{max} = 386 and 641 nm in CH_2Cl_2). The filtrate was concentrated in vacuo, and the residue was dissolved in THF (50 mL), followed by addition of decanedioic acid (7.2 mg, 0.038 mmol), *N*,*N*′-diisopropylcarbodiimide (DIC; 0.12 mL, 0.078 mmol), and 4-dimethylaminopyridine (DMAP; 11 mg, 0.090 mmol). The resulting solution was stirred for 91 h at room temperature. The mixture was filtered through a paper filter, and the filtrate was concentrated under reduced pressure. The residue was dissolved in toluene, and the resulting solution was washed with brine several times and then concentrated under reduced pressure. The residue was subjected to silica-gel column chromatography (hexane/AcOEt = 5/1). The fraction of R_f = 0.3 (hexane/AcOEt = 5/1) was collected and evaporated to give **7-C8** as an orange solid (5.0 mg, 22%). **7-C7** and **7-C9** were similarly prepared by condensation reactions of **3** with nonanedioic acid and undecanedioic acid, respectively. **7-C7**: Orange solid, 8.4 mg (20%). Mp > 300 °C. ^{1}H NMR (C_6D_6, 400 MHz): δ 6.80 (d, 4H, J = 8.3 Hz), 6.61 (t, 2H, J = 8.3 Hz), 6.50 (s, 4H), 5.72 (quint, 4H, J = 7.8 Hz), 4.52 (d, 4H, J = 4.6 Hz), 3.94 (tt, 8H, J = 8.2, 7.8 Hz), 3.59 (d, 4H, J = 4.6 Hz), 3.36 (tt, 8H, J = 8.2, 7.8 Hz), 3.11 (t, 8H, J = 8.0 Hz), 2.37 (s, 12H), 1.96 (s, 6H). HRMS (ESI) m/z: [M]$^+$ calcd for $C_{66}H_{64}N_6NiO_8$ 1126.4139; found 1126.4135. IR (ATR) ν 1769 (C═O) cm^{-1}. UV−vis (CH_2Cl_2): λ_{max} (log ε) 444 (5.00), 522 nm (4.97). **7-C8**: Mp > 300 °C. ^{1}H NMR (C_6D_6, 400 MHz): δ 6.74 (d, 4H, J = 7.6 Hz), 6.63 (t, 2H, J = 7.6 Hz), 6.51 (s, 4H), 4.75−4.65 (m, 8H), 4.50 (d, 4H, J = 4.4 Hz), 3.60 (d, 4H, J = 4.4 Hz), 3.41−3.26 (m, 8H), 3.15 (tt, 8H, J = 7.7, 7.1 Hz), 2.85 (t, 8H, J = 6.8 Hz), 2.39 (s, 12H), 1.97 (s, 6H). HRMS (ESI) m/z: [M]$^+$ calcd for $C_{68}H_{68}N_6NiO_8$ 1154.4447; found 1154.4436. IR (ATR): ν 1766 (C═O) cm^{-1}. UV−vis (CH_2Cl_2): λ_{max} (log ε) 444 (5.14), 522 nm (4.95). **7-C9**: Orange solid, 6.9 mg (12%). Mp > 300 °C. ^{1}H NMR (C_6D_6, 400 MHz): δ 6.80 (d, 4H, J = 8.3 Hz), 6.64 (t, 2H, J = 8.3 Hz), 6.51 (s, 4H), 4.50 (d, 4H, J = 4.2 Hz), 4.23 (quint, 4H, J = 7.9 Hz), 3.61 (d, 4H, J = 4.2 Hz), 3.51 (tt, 8H, J = 7.9, 7.0 Hz), 2.96 (t, 8H, J = 7.0 Hz), 2.88 (tt, 8H, J = 7.7, 7.0 Hz), 2.66 (tt, 8H, J = 7.7, 7.0 Hz), 2.36 (s, 12H), 1.97 (s, 6H). HRMS (ESI) m/z: [M]$^+$ calcd for $C_{70}H_{72}N_6NiO_8$ 1182.4765; found 1182.4757. IR (ATR): ν 1766 (C═O) cm^{-1}. UV−vis (CH_2Cl_2): λ_{max} (log ε) 443 (4.96), 523 nm (4.94). Prolonged standing of **7-Cn** (n = 7, 8, 9) in solution caused the generation of a small amount of 19π radicals, which hampered in obtaining high-quality ^{13}C NMR spectra of **7-Cn**.

Synthesis of ***8***. Typical procedure: A mixture of **7-C7** (11.2 mg, 0.0105 mmol), $AgPF_6$ (2.5 mg, 0.010 mmol), and CH_2Cl_2 (6 mL) was stirred for 2 min at room temperature. The mixture was concentrated under reduced pressure. The residue was subjected to silica-gel column chromatography (CH_2Cl_2/MeOH = 40/1). The fraction of R_f = 0.3 (CH_2Cl_2/MeOH = 20/1) was collected and evaporated to give **8-C7** as a dark-greenish-yellow solid (6.9 mg, 51%). **8-C8** and **8-C9** were similarly prepared from **7-C8** and **7-C9**, respectively. **8-C7**: Mp > 300 °C. ^{1}H NMR ($CDCl_3$, 400 MHz): δ 2.7−2.3 (br-s, 8H), 2.0−1.2 (br-s, 20H). The other ^{1}H signals were not clearly detected. ^{31}P{^{1}H} NMR ($CDCl_3$, 162 MHz): δ −144.3 (septet, $J_{P\text{-}F}$ = 712.2 Hz). HRMS (ESI) m/z: [M − PF_6]$^+$ calcd for $C_{66}H_{64}N_6NiO_8$ 1126.4134; found 1126.4126. IR (ATR): ν 1771 (C═O), 839 (P−F) cm^{-1}. UV−vis−NIR (CH_2Cl_2): λ_{max} (log ε) 380 (4.61), 439 (4.90) 914 nm (4.37). **8-C8**: Dark-greenish-yellow solid, 3.4 mg (60%). Mp > 300 °C. ^{1}H NMR (CD_2Cl_2, 400 MHz): δ 2.6−2.4 (br-s, 8H), 2.1−1.9 (br-s, 8H), 1.8−1.6 (br-s, 8H), 1.5−1.4 (br-s, 8H). The other ^{1}H signals were not clearly detected. ^{31}P{^{1}H} NMR ($CDCl_3$, 162 MHz): δ −144.4 (septet, $J_{P\text{-}F}$ = 712.8 Hz). HRMS (ESI) m/z: [M − PF_6]$^+$ calcd for $C_{68}H_{68}N_6NiO_8$ 1154.4447; found 1154.4436. IR (ATR): ν 1766 (C═O), 837 (P−F) cm^{-1}. UV−vis−NIR (CH_2Cl_2): λ_{max} (log ε) 379 (4.61), 438 (4.88), 895 nm (4.50). **8-C9**: Dark-greenish-yellow solid, 7.7 mg (74%). Mp > 300 °C. ^{1}H NMR ($CDCl_3$, 400 MHz): δ 2.7−2.3 (br-s, 8H), 2.1−1.9 (br-s, 4H), 1.8−1.2 (br-s, 24H). The other ^{1}H signals were not clearly detected. ^{31}P{^{1}H} NMR ($CDCl_3$, 162 MHz): δ −144.3 (septet, $J_{P\text{-}F}$ = 712.2 Hz). HRMS (ESI) m/z: [M − PF_6]$^+$ calcd for $C_{70}H_{72}N_6NiO_8$ 1182.4760; found 1182.4757. IR (ATR): ν 1771 (C═O), 838 (P−F) cm^{-1}. UV−vis−NIR (CH_2Cl_2): λ_{max} (log ε) 379 (4.60), 438 (4.87), 894 nm (4.52). The ^{1}H NMR spectra (400 MHz) of **8-C*n*** are shown in Figure 8.

Synthesis of ***9***. Typical procedure: A mixture of **8-C7** (5.0 mg, 4.0 μmol), $AgPF_6$ (1.1 mg, 4.4 mmol), and CH_2Cl_2 (1 mL) was stirred for 2 min at room temperature. The mixture was passed through a thin silica-gel bed, and the eluent was concentrated under reduced pressure. The residue was reprecipitated from CH_2Cl_2−hexane to give **9-C7** as a green solid (4.6 mg, 83%). **9-C8** and **9-C9** were similarly prepared from **8-C8** and **8-C9**, respectively. **9-C8** could also be prepared by oxidation of **7-C8** with two equivalents of $AgPF_6$. **9-C7**: Mp > 300 °C. ^{1}H NMR (CD_2Cl_2, 700 MHz): δ 8.85 (d, 4H, J = 4.8 Hz), 8.69 (d, 4H, J = 4.8 Hz), 8.26 (t, 2H, J = 8.2 Hz), 7.80 (d, 4H, J = 8.2 Hz), 7.38 (s, 4H), 2.61 (s, 6H), 1.89 (s, 12H), 1.76 (t, 8H, J = 7.6 Hz), 0.26 (tt, 8H, J = 7.6, 7.6 Hz), −0.51 (quint, 4H, J = 7.6 Hz), −1.60 to −1.70 (m, 8H). HRMS (ESI) m/z: [M − 2 PF_6 + H_2O]$^{z+}$ calcd for $C_{66}H_{66}N_6NiO_9$ 1126.4134 (z = 1), 572.7156 (z = 2); found 1126.4126 (z = 1), 572.7145 (z = 2). IR (ATR): ν 1767 (C═O), 837 (P−F) cm^{-1}. UV−vis (CH_2Cl_2): λ_{max} (relative intensity) 397 (1), 651 nm (0.45). **9-C8**: Green solid, 3.7 mg (63%). Mp 252−254 °C. ^{1}H NMR (CD_2Cl_2, 400 MHz): δ 8.86 (d, 4H, J = 5.2 Hz), 8.63 (d, 4H, J = 5.2 Hz), 8.21 (t, 2H, J = 8.4 Hz), 7.75 (d, 4H, J = 8.4 Hz), 7.34 (s, 4H), 2.58 (s, 6H), 1.92 (t, 8H, J = 7.2 Hz), 1.83 (s, 12H), 0.06 (tt, 8H, J = 7.6, 7.2 Hz), −0.61 to −0.64 (m, 8H), −0.73 to −0.82 (m, 8H). ^{31}P{^{1}H} NMR ($CDCl_3$, 162 MHz): δ −144.9 (septet, $J_{P\text{-}F}$ = 708.3 Hz). HRMS (ESI) m/z: [M − 2 PF_6]$^{z+}$ calcd for $C_{68}H_{68}N_6NiO_8$ 1154.4447 (z = 1), 577.2221 (z = 2); found 1154.4456 (z = 1), 577.2207 (z = 2). IR (ATR): ν 1769 (C═O), 837 (P−F) cm^{-1}. UV−vis (CH_2Cl_2): λ_{max} (relative intensity) 394 (1), 634 nm (0.46). **9-C9**: Green solid, 4.2 mg (86%). Mp > 300 °C. ^{1}H NMR (CD_2Cl_2, 700 MHz): δ 8.77 (d, 4H, J = 5.3 Hz), 8.58 (d, 4H, J = 5.3 Hz), 8.15 (t, 2H, J = 8.6 Hz), 7.69 (d, 4H, J = 8.6 Hz), 7.32 (s, 4H), 2.58 (s, 6H), 1.89 (t, 8H, J = 7.0 Hz), 1.83 (s, 12H), 0.82 (tt, 8H, J = 7.7, 7.0 Hz), −0.14 (tt, 8H, J = 7.7, 7.7 Hz), −0.24 (tt, 8H, J = 7.7, 7.7 Hz), −0.29 (quint, 4H, J = 7.7 Hz). HRMS (ESI) m/z: [M − 2 PF_6]$^{z+}$ calcd for $C_{70}H_{72}N_6NiO_8$ 1182.4760 (z = 1), 592.2455 (z = 2); found 1182.4757 (z = 1), 593.2371 (z = 2). IR (ATR): ν 1770 (C═O), 835 (P−F) cm^{-1}. UV−vis (CH_2Cl_2): λ_{max} (relative intensity) 397 (1), 631 nm (0.56). Prolonged standing of **9-Cn** (n = 7, 8, 9) in solution caused the generation of a small amount of 19π radicals, which hampered in obtaining high-quality ^{13}C NMR spectra of **9-Cn**.

Synthesis of ***10***. This compound was prepared from 2,6-dimethoxybenzaldehyde and pyrrole according to the reported procedure.[35] ^{1}H NMR ($CDCl_3$, 400 MHz): δ 8.92 (d, 4H, J = 4.6 Hz), 8.79 (d, 4H, J = 4.6 Hz), 7.63 (t, 2H, J = 8.4 Hz), 7.30 (s, 4H), 7.00 (d, 4H, J = 8.4 Hz), 4.70 (s, 4H), 2.64 (s, 6H), 1.84 (s, 12H), −2.61 (br-s, 2H).

Synthesis of ***11***. A mixture of **10** (110 mg, 0.144 mmol), $Ni(OAc)_2{\cdot}4H_2O$ (111 mg, 0.444 mmol), and DMF (5 mL) was stirred for 19 h at 140 °C. After being quenched with water, the precipitated solid was filtered, and the residue was washed with water (100 mL × 8) and dissolved in CH_2Cl_2, and the solution was evaporated under reduced pressure. The residue was then reprecipitated from CH_2Cl_2−hexane to give **11** as a pink solid (104 mg, 88%). Mp > 300 °C. ^{1}H NMR ($CDCl_3$, 400 MHz): δ 8.82 (d, 4H, J = 5.0 Hz), 8.69 (d, 4H, J = 5.0 Hz), 7.56 (t, 2H, J = 8.0 Hz), 7.23 (s, 4H), 6.93 (d, 4H, J = 8.0 Hz), 4.67 (br-s, 4H), 2.59 (s, 6H), 1.81 (s, 12H). ^{13}C{^{1}H} NMR ($CDCl_3$, 100 MHz): δ 155.9, 143.6, 143.1, 138.8, 138.1, 136.3, 133.1, 131.9, 131.1, 127.9, 118.6, 114.3, 107.8, 104.4, 21.4. HRMS (ESI) m/z: [M]$^+$ calcd for $C_{50}H_{40}N_4NiO_4$ 818.2398; found 818.2403. UV−vis (CH_2Cl_2): λ_{max} (log ε) 411 (5.53), 525 (4.54), 556 nm (4.08).

Synthesis of ***12***. A mixture of **11** (30.0 mg, 0.0392 mmol), acetic anhydride (0.10 mL, 1.1 mmol), pyridine (50 μL, 0.96 mmol), and CH_2Cl_2 (3 mL) was stirred for 24 h at room temperature. After being quenched with water, the aqueous layer was extracted with CH_2Cl_2, and the combined organic extracts were subsequently washed with aqueous HCl and $NaHCO_3$ solutions, dried over Na_2SO_4, and

https://dx.doi.org/10.1021/acs.joc.0c02433
J. Org. Chem. 2021, 86, 2283−2296

evaporated under reduced pressure. The residue was subjected to silica-gel column chromatography (hexane/EtOAc = 10/1). The fraction of R_f = 0.3 (hexane/EtOAc = 10/1) was collected and evaporated to leave a solid residue, which was reprecipitated from hexane−CH_2Cl_2 to give **12** as a purple solid (27.6 mg, 71%). Mp > 300 °C. ^{1}H NMR ($CDCl_3$, 400 MHz): δ 8.65 (d, 4H, J = 4.8 Hz), 8.58 (d, 4H, J = 4.8 Hz), 7.82 (t, 2H, J = 8.3 Hz), 7.46 (d, 4H, J = 8.3 Hz), 7.22 (s, 4H), 2.59 (s, 6H), 1.79 (s, 12H), 1.14 (s, 12H). ^{13}C{^{1}H} NMR ($CDCl_3$, 100 MHz): δ 168.6, 151.3, 143.2, 143.0, 138.7, 137.9, 137.1, 131.6, 131.1, 129.7, 127.8, 127.5, 120.5, 117.6, 108.2, 21.4, 21.3, 20.1. HRMS (ESI) m/z: $[M]^+$ calcd for $C_{58}H_{48}N_4NiO_8$ 986.2820; found 986.2815. IR (ATR): ν 1761 (C═O) cm^{-1}. UV−vis (CH_2Cl_2): λ_{max} (log ε) 412 (5.57), 527 (4.43), 559 nm (4.05).

Synthesis of ***13***. Typical procedure: A mixture of **11** (31.7 mg, 0.0387 mmol), decanedioyl dichloride (17.9 mg, 0.0749 mmol), triethylamine (0.03 mL, 0.2 mmol), and CH_2Cl_2 (110 mL) was stirred for 39 h at room temperature. The mixture was then passed through a paper filter, and the filtrate was concentrated under reduced pressure. The residue was subjected to silica-gel column chromatography (hexane/AcOEt = 5/1). The fraction of R_f = 0.3 (hexane/AcOEt = 5/1) was collected and reprecipitated from CH_2Cl_2−hexane to give **13-C8** as a purple solid (7.0 mg, 16%). **13-C7** and **13-C9** were similarly prepared by acylation of **11** with two equivalents of nonanedioyl dichloride and undecanedioyl dichloride, respectively. **13-C7**: Purple solid, 24.1 mg (23%). Mp > 300 °C. ^{1}H NMR ($CDCl_3$, 400 MHz): δ 8.65 (d, 4H, J = 5.0 Hz), 8.58 (d, 4H, J = 5.0 Hz), 7.84 (t, 2H, J = 8.0 Hz), 7.47 (d, 4H, J = 8.0 Hz), 7.23 (s, 4H), 2.59 (s, 6H), 1.78 (s, 12H), 1.20 (t, 8H, J = 7.6 Hz), −1.18 (tt, 8H, J = 7.6, 7.6 Hz), −1.39 (tt, 8H, J = 7.2, 7.6 Hz), −1.74 (quint, 4H, J = 7.2 Hz). ^{1}H NMR (CD_2Cl_2, 700 MHz): δ 8.61 (d, 4H, J = 4.9 Hz), 8.55 (d, 4H, J = 4.9 Hz), 7.86 (t, 2H, J = 8.4 Hz), 7.47 (d, 4H, J = 8.4 Hz), 7.26 (s, 4H), 2.59 (s, 6H), 1.79 (s, 12H), 1.16 (t, 8H, J = 7.9 Hz), −1.07 (tt, 8H, J = 8.1, 7.9 Hz), −1.57 (tt, 8H, J = 8.1, 8.1 Hz), −1.67 (quint, 4H, J = 8.1 Hz). ^{13}C{^{1}H} NMR ($CDCl_3$, 100 MHz): δ 171.2, 151.9, 143.3, 143.1, 138.5, 137.8, 137.3, 132.0, 130.9, 130.7, 129.1, 127.8, 120.5, 117.4, 108.4, 33.5, 29.6, 27.1, 24.3, 21.4, 21.3. HRMS (ESI) m/z: $[M]^+$ calcd for $C_{68}H_{64}N_4NiO_8$ 1122.4072; found 1122.4077. IR (ATR): ν 1762 (C═O) cm^{-1}. UV−vis (CH_2Cl_2): λ_{max} (log ε) 410 (5.55), 524 (4.42), 558 nm (4.12). **13-C8**: Mp > 300 °C. ^{1}H NMR ($CDCl_3$, 400 MHz): δ 8.70 (d, 4H, J = 4.8 Hz), 8.57 (d, 4H, J = 4.8 Hz), 7.83 (t, 2H, J = 8.3 Hz), 7.42 (d, 4H, J = 8.3 Hz), 7.22 (s, 4H), 2.59 (s, 6H), 1.79 (s, 12H), 1.68 (t, 8H, J = 6.8 Hz), −0.57 (tt, 8H, J = 6.8, 7.6 Hz), −1.47 to −1.58 (m, 8H), −1.70 to −1.80 (m, 8H). ^{1}H NMR (CD_2Cl_2, 400 MHz): δ 8.66 (d, 4H, J = 4.8 Hz), 8.56 (d, 4H, J = 4.8 Hz), 7.85 (t, 2H, J = 8.3 Hz), 7.42 (d, 4H, J = 8.3 Hz), 7.26 (s, 4H), 2.59 (s, 6H), 1.79 (s, 12H), 1.66 (t, 8H, J = 6.9 Hz), −0.56 (tt, 8H, J = 7.6, 6.9 Hz), −1.50 to −1.60 (m, 8H), −1.64 to −1.77 (m, 8H). ^{13}C{^{1}H} NMR ($CDCl_3$, 100 MHz): δ 171.3, 151.5, 143.3, 143.1, 138.7, 137.7, 137.4, 131.9, 130.8, 130.0, 128.6, 127.8, 120.5, 117.6, 108.0, 34.8, 27.5, 27.2, 23.8, 21.5, 21.4. HRMS (ESI) m/z: $[M]^+$ calcd for $C_{70}H_{68}N_4NiO_8$ 1150.4385; found 1150.4382. IR (ATR): ν 1758 (C═O) cm^{-1}. UV−vis (CH_2Cl_2): λ_{max} (log ε) 411 (5.51), 524 (4.40), 558 nm (4.08). **13-C9**: Purple solid, 10.6 mg (24%). Mp > 300 °C. ^{1}H NMR ($CDCl_3$, 400 MHz): δ 8.69 (d, 4H, J = 4.8 Hz), 8.57 (d, 4H, J = 4.8 Hz), 7.81 (t, 2H, J = 8.4 Hz), 7.42 (d, 4H, J = 8.3 Hz), 7.21 (s, 4H), 2.59 (s, 6H), 1.78 (s, 12H), 1.63 (t, 8H, J = 7.0 Hz), 0.07−0.04 (m, 8H), −0.98 − −1.14 (m, 16H), −1.45 (quint, 4H, J = 6.4 Hz). ^{1}H NMR (CD_2Cl_2, 700 MHz): δ 8.65 (d, 4H, J = 4.9 Hz), 8.54 (d, 4H, J = 4.9 Hz), 7.82 (t, 2H, J = 9.0 Hz), 7.42 (d, 4H, J = 9.0 Hz), 7.24 (s, 4H), 2.57 (s, 6H), 1.78 (s, 12H), 1.60 (t, 8H, J = 6.3 Hz), 0.08 (tt, 8H, J = 7.0, 6.3 Hz), −1.00 to −1.12 (m, 16H), −1.42 (quint, 4H, J = 6.4 Hz). ^{13}C{^{1}H} NMR ($CDCl_3$, 100 MHz): δ 171.4, 151.5, 143.0, 142.8, 138.7, 137.7, 137.4, 131.9, 130.9, 129.7, 128.0, 127.8, 120.4, 117.4, 108.1, 33.2, 26.3, 25.6, 23.9, 23.1, 21.5, 21.4. HRMS (ESI) m/z: $[M]^+$ calcd for $C_{72}H_{72}N_4NiO_8$ 1178.4698; found 1178.4711. IR (ATR) ν 1759 (C═O) cm^{-1}. UV−vis (CH_2Cl_2): λ_{max} (log ε) 411 (5.61), 524 (4.45), 558 nm (4.01).

Synthesis of ***14***. Typical procedure: A mixture of phenol (174 mg, 1.85 mmol), decanedioyl dichloride (218 mg, 0.913 mmol), triethylamine (0.40 mL, 2.9 mmol), and CH_2Cl_2 (35 mL) was stirred for 16 h at room temperature. After being quenched with ice-water, the aqueous layer was extracted with Et_2O, and the combined organic extracts were washed with brine, dried over Na_2SO_4, and evaporated under reduced pressure. The residue was then subjected to silica-gel column chromatography (hexane/AcOEt = 5/1). The fraction of R_f = 0.6 (hexane/AcOEt = 5/1) was collected and evaporated to give **14-C8** as a colorless solid (78 mg, 45%). **14-C7** and **14-C9** were similarly prepared by reactions of phenol with nonanedioyl dichloride and undecanedioyl dichloride, respectively. **14-C7**: Colorless solid. 78.1 mg (45%). Mp 69−71 °C. ^{1}H NMR ($CDCl_3$, 400 MHz): δ 7.39 (t, 4H, J = 7.8 Hz), 7.23 (t, 2H, J = 7.8 Hz), 7.08 (d, 4H, J = 7.8 Hz), 2.58 (t, 4H, J = 7.6 Hz), 1.79 (tt, 4H, J = 7.6, 7.6 Hz), 1.49−1.45 (m, 6H). ^{1}H NMR (C_6D_6, 700 MHz): δ 7.12 (d, 4H, J = 8.1 Hz), 7.08 (t, 4H, J = 8.1 Hz), 6.92 (t, 2H, J = 8.1 Hz), 2.24 (t, 4H, J = 7.4 Hz), 1.55 (tt, 4H, J = 7.7, 7.4 Hz), 1.14 (tt, 4H, J = 7.7, 7.7 Hz), 1.10 (quint, 2H, J = 7.7 Hz). ^{1}H NMR (CD_2Cl_2, 700 MHz): δ 7.39 (t, 4H, J = 7.8 Hz), 7.24 (t, 2H, J = 7.8 Hz), 7.08 (d, 4H, J = 7.8 Hz), 2.56 (t, 4H, J = 7.6 Hz), 1.75 (tt, 4H, J = 7.6 Hz), 1.46−1.42 (m, 6H). ^{13}C{^{1}H} NMR (C_6D_6, 100 MHz): δ 171.8, 151.9, 129.9, 126.1, 122.3, 34.7, 29.5, 29.4, 25.4. HRMS (ESI) m/z: $[M + H]^+$ calcd for $C_{21}H_{25}O_4$ 341.1747; found 341.1747. IR (ATR): ν 1749 (C═O) cm^{-1}. **14-C8**: Mp 68−70 °C. ^{1}H NMR (700 MHz, $CDCl_3$): δ 7.38 (t, 4H, J = 8.1 Hz), 7.23 (t, 2H, J = 8.1 Hz), 7.09 (d, 4H, J = 8.1 Hz), 2.57 (t, 4H, J = 7.0 Hz), 1.78 (tt, 4H, J = 7.7, 7.0 Hz), 1.45−1.43 (m, 4H), 1.41−1.40 (m, 4H). ^{1}H NMR (C_6D_6, 700 MHz): δ 7.12−7.10 (d, 4H, J = 8.1 Hz), 7.09−7.06 (t, 4H, J = 7.0 Hz), 6.92 (t, 2H, J = 7.7 Hz), 2.26 (t, 4H, J = 7.0 Hz), 1.56 (tt, 4H, J = 7.7, 7.0 Hz), 1.20−1.16 (m, 4H), 1.14−1.12 (m, 4H). ^{1}H NMR (CD_2Cl_2, 700 MHz): δ 7.38 (t, 4H, J = 8.1 Hz), 7.23 (t, 2H, J = 8.1 Hz), 7.07 (d, 4H, J = 8.1 Hz), 2.55 (t, 4H, J = 7.0, 7.7 Hz), 1.74 (tt, 4H, J = 7.0, 7.7 Hz), 1.44−1.42 (m, 4H), 1.40−1.38 (m, 4H). ^{13}C{^{1}H} NMR (C_6D_6, 100 MHz): δ 171.8, 151.9, 129.9, 126.0, 122.3, 34.7, 29.7, 29.6, 25.5. HRMS (ESI) m/z: $[M + H]^+$ calcd for $C_{22}H_{27}O_4$ 355.1904; found 355.1899. IR (ATR): ν 1745 (C═O) cm^{-1}. **14-C9**: Colorless solid. 71.4 mg (38%). Mp 68−70 °C. ^{1}H NMR ($CDCl_3$, 400 MHz): δ 7.39 (t, 4H, J = 8.1 Hz), 7.23 (t, 2H, J = 8.1 Hz), 7.09 (d, 4H, J = 8.1 Hz), 2.57 (t, 4H, J = 7.4 Hz), 1.77 (tt, 4H, J = 7.7, 7.4 Hz), 1.50−1.34 (m, 10H). ^{1}H NMR (C_6D_6, 700 MHz): δ 7.11 (d, 4H, J = 7.8 Hz), 7.08 (t, 4H, J = 7.8 Hz), 6.92 (t, 2H, J = 7.8 Hz), 2.27 (t, 4H, J = 7.7 Hz), 1.61 (tt, 4H, J = 7.7, 7.4 Hz), 1.23−1.19 (m, 4H), 1.18−1.14 (m, 6H). ^{1}H NMR (CD_2Cl_2, 700 MHz): δ 7.39 (t, 4H, J = 8.1 Hz), 7.24 (t, 2H, J = 8.1 Hz), 7.07 (d, 4H, J = 8.1 Hz), 2.55 (t, 4H, J = 7.2 Hz), 1.74 (tt, 4H, J = 7.7, 7.2 Hz), 1.44−1.39 (m, 4H), 1.38−1.33 (m, 6H). ^{13}C{^{1}H} NMR (C_6D_6, 100 MHz): δ 172.0, 152.2, 130.2, 126.3, 122.6, 35.0, 30.2, 30.1, 29.9, 25.8. HRMS (ESI) m/z: $[M + H]^+$ calcd for $C_{23}H_{29}O_4$ 369.2060; found 369.2060. IR (ATR): ν 1748 (C═O) cm^{-1}.

Density Functional Theory Calculations. The geometries were optimized with the density functional theory (DFT) method (for details, see the main text). The basis sets used for the optimization were the 6−311G(d,p) basis set[47] for H, C, and N and the Wachters−Hay all-electron basis set[48] supplemented with one f-function (exponent: 1.29 for Ni, 1.62 for Zn). The functional of DFT was the Becke, three-parameter, Lee−Yang−Parr (B3LYP) exchange-correlation functional.[49] The optimized geometries were confirmed to be minima by vibrational analysis. The Cartesian coordinates and computed total energies are summarized in Table S3 in the SI. The nucleus-independent chemical shift (NICS) was calculated at the Hartree−Fock level with gauge-including atomic orbitals (GIAOs) at the DFT-optimized geometries. The basis set used for the NICS calculations was 6-31+G(d).[50] All of the calculations were carried out using the Gaussian 16 suite of programs.[51]

Electron Paramagnetic Resonance Measurements. The EPR spectra of 19π TADAPs **4** and **8-C*n*** were measured at room temperature. All samples were prepared as a 0.1 mM solution in CH_2Cl_2. After three freeze−pump−thaw cycles, the solution sample in a quartz tube was sealed by frame. Spectral simulation was performed using EasySpin,[52] which is a MATLAB toolbox meant for

https://dx.doi.org/10.1021/acs.joc.0c02433
J. Org. Chem. 2021, 86, 2283−2296

this. The static magnetic field and microwave frequency were measured by a gauss meter.

■ ASSOCIATED CONTENT

Supporting Information

The Supporting Information is available free of charge at https://pubs.acs.org/doi/10.1021/acs.joc.0c02433.

NMR and EPR spectra, data of DFT calculations, and additional figures and tables (PDF)

■ AUTHOR INFORMATION

Corresponding Author

Yoshihiro Matano − *Department of Chemistry, Faculty of Science, Niigata University, Nishi-ku, Niigata 950-2181, Japan;* orcid.org/0000-0003-3377-0004; Email: matano@chem.sc.niigata-u.ac.jp

Authors

Hikari Ochiai − *Department of Chemistry, Graduate School of Science and Technology, Niigata University, Nishi-ku, Niigata 950-2181, Japan*

Ko Furukawa − *Center for Coordination of Research Facilities, Institute for Research Promotion, Niigata University, Nishi-ku, Niigata 950-2181, Japan; Institute for Molecular Science, Okazaki 444-8585, Japan*

Haruyuki Nakano − *Department of Chemistry, Graduate School of Science, Kyushu University, Fukuoka 819-0395, Japan;* orcid.org/0000-0002-7008-0312

Complete contact information is available at: https://pubs.acs.org/10.1021/acs.joc.0c02433

Notes

The authors declare no competing financial interest.

■ ACKNOWLEDGMENTS

The authors gratefully thank Prof. Mao Minoura (Rikkyo University) for his kind and continuous support regarding X-ray crystallographic analyses. This work was financially supported by JSPS KAKENHI (18H01961 to Y.M., 18K05036 to H.N.) and Union Tool foundation (Y.M.).

■ REFERENCES

(1) Minkin, V. I.; Glukhovtsev, M. N.; Simkin, B. Y. Aromaticity and Antiaromaticity. In *Electronic and Structural Aspects*; John Wiley & Sons: New York, 1994.

(2) Krygowski, T. M.; Cyrański, M. K.; Czarnocki, Z.; Häfelinger, G.; Katritzky, A. R. Aromaticity: A Theoretical Concept of Immense Practical Importance. *Tetrahedron* **2000**, *56*, 1783−1796.

(3) Gomes, J. A. N. F.; Mallion, R. B. Aromaticity and Ring Currents. *Chem. Rev.* **2001**, *101*, 1349−1384.

(4) Krygowski, T. M.; Cyrański, M. K. Structural Aspects of Aromaticity. *Chem. Rev.* **2001**, *101*, 1385−1419.

(5) Cyrański, M. K. Energetic Aspects of Cyclic Pi-Electron Delocalization: Evaluation of the Methods of Estimating Aromatic Stabilization Energies. *Chem. Rev.* **2005**, *105*, 3773−3811.

(6) Spitler, E. L.; Johnson, C. A., II; Haley, M. M. Renaissance of Annulene Chemistry. *Chem. Rev.* **2006**, *106*, 5344−5386.

(7) Sessler, J. L.; Seidel, D. Synthetic Expanded Porphyrin Chemistry. *Angew. Chem., Int. Ed.* **2003**, *42*, 5134−5175.

(8) Yoon, Z. S.; Osuka, A.; Kim, D. Möbius Aromaticity and Antiaromaticity in Expanded Porphyrins. *Nat. Chem.* **2009**, *1*, 113−122.

(9) Shin, J.-Y.; Kim, K. S.; Yoon, M.-C.; Lim, J. M.; Yoon, Z. S.; Osuka, A.; Kim, D. Aromaticity and Photophysical Properties of Various Topology-controlled Expanded Porphyrins. *Chem. Soc. Rev.* **2010**, *39*, 2751−2767.

(10) Hiroto, S.; Shinokubo, H. Syntheses and Properties of Antiaromatic Porphyrinoids. In *Handbook of Porphyrin Science*; Kadish, K. M.; Smith, K. M.; Guilard, R., Eds.; World Scientific: Singapore, 2016; Vol. 37, pp 233−302.

(11) Reddy, B. K.; Basavarajappa, A.; Ambhore, M. D.; Anand, V. G. Isophlorinoids: The Antiaromatic Congeners of Porphyrinoids. *Chem. Rev.* **2017**, *117*, 3420−3443.

(12) (a) Peeks, M. D.; Claridge, T. D. W.; Anderson, H. L. Aromatic and Antiaromatic Ring Currents in A Molecular Nanoring. *Nature* **2017**, *541*, 200−203. (b) Peeks, M. D.; Jirasek, M.; Claridge, T. D. W.; Anderson, H. L. Global Aromaticity and Antiaromaticity in Porphyrin Nanoring Anions. *Angew. Chem., Int. Ed.* **2019**, *58*, 15717−15720.

(13) (a) Gershoni-Poranne, R.; Stanger, A. Magnetic Criteria of Aromaticity. *Chem. Soc. Rev.* **2015**, *44*, 6597−6615. (b) Mitchell, R. H.; Iyer, V. S.; Khalifa, N.; Mahadevan, R.; Venugopalan, S.; Weerawarna, S. A.; Zhou, P. An Experimental Estimation of Aromaticity Relative to That of Benzene. The Synthesis and NMR Properties of a Series of Highly Annelated Dimethyldihydropyrenes: Bridged Benzannulenes. *J. Am. Chem. Soc.* **1995**, *117*, 1514−1532. (c) Mitchell, R. H. Measuring Aromaticity by NMR. *Chem. Rev.* **2001**, *101*, 1301−1316.

(14) Cosmo, R.; Kautz, C.; Meerholz, K.; Heinze, J.; Müllen, K. Highly Reduced Porphyrins. *Angew. Chem., Int. Ed.* **1989**, *28*, 604−607.

(15) Pohl, M.; Schmickler, H.; Lex, J.; Vogel, E. Isophlorins: Molecules at the Crossroads of Porphyrin and Annulene Chemistry. *Angew. Chem., Int. Ed.* **1991**, *30*, 1693−1697.

(16) Setsune, J.; Kashihara, K.; Wada, K.; Shiozaki, H. Photoreduction of *N,N′*-Bridged Porphyrins to 20π Antiaromatic Isophlorins. *Chem. Lett.* **1999**, *28*, 847−848.

(17) Vaid, T. P. A Porphyrin with a C=C Unit at Its Center. *J. Am. Chem. Soc.* **2011**, *133*, 15838−15841.

(18) Kon-no, M.; Mack, J.; Kobayashi, N.; Suenaga, M.; Yoza, K.; Shinmyozu, T. Synthesis, Optical Properties, and Electronic Structures of Fully Core-modified Porphyrin Dications and Isophlorins. *Chem. − Eur. J.* **2012**, *18*, 13361−13371.

(19) (a) Reddy, J. S.; Anand, V. G. Planar *Meso* Pentafluorophenyl Core Modified Isophlorins. *J. Am. Chem. Soc.* **2008**, *130*, 3718−3719. (b) Reddy, B. K.; Gadekar, S. C.; Anand, V. G. Non-covalent composites of antiaromatic isophlorin−fullerene. *Chem. Commun.* **2015**, *51*, 8276−8279. (c) Panchal, S. P.; Gadekar, S. C.; Anand, V. G. Controlled Core-Modification of a Porphyrin into an Antiaromatic Isophlorin. *Angew. Chem., Int. Ed.* **2016**, *55*, 7797−7800.

(20) Nakabuchi, T.; Nakashima, M.; Fujishige, S.; Nakano, H.; Matano, Y.; Imahori, H. Synthesis and Reactions of Phosphaporphyrins: Reconstruction of π-Skeleton Triggered by Oxygenation of a Core Phosphorus Atom. *J. Org. Chem.* **2010**, *75*, 375−389.

(21) Liu, C.; Shen, D.-M.; Chen, Q.-Y. Synthesis and Reactions of 20π-Electron β-Tetrakis(trifluoromethyl)-*meso*-tetraphenylporphyrins. *J. Am. Chem. Soc.* **2007**, *129*, 5814−5815.

(22) (a) Cissell, J. A.; Vaid, T. P.; Rheingold, A. L. An Antiaromatic Porphyrin Complex: Tetraphenylporphyrinato(silicon)$(L)_2$ (L = THF or Pyridine). *J. Am. Chem. Soc.* **2005**, *127*, 12212−12213. (b) Cissell, J. A.; Vaid, T. P.; Yap, G. P. A. Reversible Oxidation State Change in Germanium(tetraphenylporphyrin) Induced by a Dative Ligand: Aromatic Ge^{II}(TPP) and Antiaromatic Ge^{IV}(TPP)-$(pyridine)_2$. *J. Am. Chem. Soc.* **2007**, *129*, 7841−7847.

(23) (a) Weiss, A.; Hodgson, M. C.; Boyd, P. D. W.; Siebert, W.; Brothers, P. J. Diboryl and Diboranyl Porphyrin Complexes: Synthesis, Structural Motifs, and Redox Chemistry: Diborenyl Porphyrin or Diboranyl Isophlorin? *Chem. − Eur. J.* **2007**, *13*, 5982−5993. (b) Brothers, P. J. Boron Complexes of Porphyrins and Related Polypyrrole Ligands: Unexpected Chemistry for Both Boron and the Porphyrin. *Chem. Commun.* **2008**, 2090−2102.

(24) Matano, Y.; Nakabuchi, T.; Fujishige, S.; Nakano, H.; Imahori, H. Redox-Coupled Complexation of 23-Phospha-21-thiaporphyrin

with Group 10 Metals: A Convenient Access to Stable Core-Modified Isophlorin−Metal Complexes. *J. Am. Chem. Soc.* **2008**, *130*, 16446−16447.
(25) Ishii, K.; Kobayashi, N. The Photophysical Properties of Phthalocyanines and Related Compounds. In *The Porphyrin Handbook*; Kadish, K. M.; Smith, K. M.; Guilard, R., Eds.; Academic Press: San Diego, 2003; Vol. *16*, pp 1−42.
(26) Mack, J.; Kobayashi, N. Low Symmetry Phthalocyanines and Their Analogues. *Chem. Rev.* **2011**, *111*, 281−321.
(27) Matano, Y. Synthesis of Aza-, Oxa-, and Thiaporphyrins and Related Compounds. *Chem. Rev.* **2017**, *117*, 3138−3191.
(28) (a) Matano, Y.; Shibano, T.; Nakano, H.; Imahori, H. Nickel(II) and Copper(II) Complexes of *β*-Unsubstituted 5,15-Diazaporphyrins and Pyridazine-Fused Diazacorrinoids: Metal-Template Syntheses and Peripheral Functionalizations. *Chem. − Eur. J.* **2012**, *18*, 6208−6216. (b) Matano, Y.; Shibano, T.; Nakano, H.; Kimura, Y.; Imahori, H. Free Base and Metal Complexes of 5,15-Diaza-10,20-dimesitylporphyrins: Synthesis, Structures, Optical and Electrochemical Properties, and Aromaticities. *Inorg. Chem.* **2012**, *51*, 12879−12890.
(29) Satoh, T.; Minoura, M.; Nakano, H.; Furukawa, K.; Matano, Y. Redox-Switchable 20*π*-, 19*π*-, and 18*π*-Electron 5,10,15,20-Tetraaryl-5,15-diazaporphyrinoid Nickel(II) Complexes. *Angew. Chem., Int. Ed.* **2016**, *55*, 2235−2238.
(30) Sudoh, K.; Satoh, T.; Amaya, T.; Furukawa, K.; Minoura, M.; Nakano, H.; Matano, Y. Syntheses, Properties, and Catalytic Activities of Metal(II) Complexes and Free Bases of Redox-Switchable 20*π*, 19*π*, and 18*π* 5,10,15,20-Tetraaryl-5,15-diazaporphyrinoids. *Chem. − Eur. J.* **2017**, *23*, 16364−16373.
(31) Sudoh, K.; Satoh, Y.; Furukawa, K.; Nakano, H.; Matano, Y. Synthesis and Optical, Magnetic, and Electrochemical Properties of 5,10,15,20-Tetraaryl-5,15-diazaporphyrin−Tertiary Amine Conjugates. *J. Porphyrins Phthalocyanines* **2020**, *24*, 286−297.
(32) Related diazaporphyrinoids: (a) Sudoh, K.; Hatakeyama, T.; Furukawa, K.; Nakano, H.; Matano, Y. Redox Switchable 19*π* and 18*π* 5,10,20-Triaryl-5,15-diazaporphyrinoid−Nickel(II) Complexes. *J. Porphyrins Phthalocyanines* **2018**, *22*, 542−551. (b) Mutoh, M.; Sudoh, K.; Furukawa, K.; Minoura, M.; Nakano, H.; Matano, Y. Synthesis of Redox-Switchable 5,15-Dialkyl-10,20-diaryl-5,15-diazaporphyrins and Diversification of Their *N*-Alkyl Groups. *Asian J. Org. Chem.* **2019**, *8*, 352−355. (c) Yamaji, A.; Tsurugi, H.; Miyake, Y.; Mashima, K.; Shinokubo, H. Chemo- and Regioselective Reduction of 5,15-Diazaporphyrins Providing Antiaromatic Azaporphyrinoids. *Chem. − Eur. J.* **2016**, *22*, 3956−3961. (d) Chia, W. X.; Nishijo, M.; Kang, S.; Oh, J.; Nishimura, T.; Omori, H.; Longevial, J.-F.; Miyake, Y.; Kim, D.; Shinokubo, H. Site-Selective N-Methylation of 5,15-Diazaporphyrins: Reactive Cationic Porphyrinoids that Provide Isoporphyrin Analogues. *Chem. − Eur. J.* **2020**, *26*, 2754−2760.
(33) Recently, Anderson and coworkers used strapped porphyrins as indicators for the evaluation of aromatic characters of porphyrin nanorings. Roche, C.; Luo, Q.; Gil-Ramírez, G.; Jiang, H.-W.; Kohn, D. R.; Xiong, Y.; Thompson, A. L.; Anderson, H. L. Unexpected Interactions between Alkyl Straps and Pyridine Ligands in Sulfur-Strapped Porphyrin Nanorings. *J. Org. Chem.* **2017**, *82*, 7446−7462.
(34) The C7-strapped derivatives could not be completely purified by column chromatography and recrystallization; the ^{1}H NMR spectra of **7-C7** and **9-C7** showed the presence of uncharacterized impurities. However, the amount of the impurities is so small that it does not affect the following discussion about the optical, electrochemical, and magnetic properties of the C7-strapped derivatives.
(35) Kuijpers, P. F.; Tiekink, M. J.; Breukelaar, W. B.; Broere, D. L. J.; van Leest, N. P.; van der Vlugt, J. I.; Reek, J. N. H.; de Bruin, B. Cobalt-Porphyrin-Catalysed Intramolecular Ring-Closing C−H Amination of Aliphatic Azides: A Nitrene-Radical Approach to Saturated Heterocycles. *Chem. − Eur. J.* **2017**, *23*, 7945−7952.
(36) Single crystals of **7-C8** and **7-C9** were grown from hexane−CH_2Cl_2 and cyclohexane−CH_2Cl_2, respectively. The currently available crystallographic data clearly show the whole structures of both compounds, although their quality is not at a publishable level. Therefore, we do not include the crystal structures and their data in this paper. Preliminary results of X-ray analyses were included during the review process.
(37) Schleyer, P. v. R.; Maerker, C.; Dransfeld, A.; Jiao, H.; van Eikema Hommes, N. J. R. Nucleus-Independent Chemical Shifts: A Simple and Efficient Aromaticity Probe. *J. Am. Chem. Soc.* **1996**, *118*, 6317−6318.
(38) Cyrañski, M. K.; Krygowski, T. M.; Wisiorowski, M.; van Eikema Hommes, N. J. R.; Schleyer, P. v. R. Global and Local Aromaticity in Porphyrins: An Analysis Based on Molecular Geometries and Nucleus-Independent Chemical Shifts. *Angew. Chem., Int. Ed.* **1998**, *37*, 177−180.
(39) Chen, Z.; Wannere, C. S.; Corminboeuf, C.; Puchta, R.; Schleyer, P. v. R. Nucleus-Independent Chemical Shifts (NICS) as an Aromaticity Criterion. *Chem. Rev.* **2005**, *105*, 3842−3888.
(40) Fallah-Bagher-Shaidaei, H.; Wannere, C. S.; Corminboeuf, C.; Puchta, R.; Schleyer, P. v. R. Which NICS Aromaticity Index for Planar *π* Rings Is Best? *Org. Lett.* **2006**, *8*, 863−866.
(41) Stanger, A. NICS − Past and Present. *Eur. J. Org. Chem.* **2020**, *2020*, 3120−3127.
(42) Stanger reported a NICS-scan method in which the chemical shifts of a probe are scanned over a distance above the center of the molecular plane and dissected into their in-plane and out-of-plane components. His group also showed that NICSzz provides qualitative pictures as the identification of global ring currents at a height of 1.7 Å above the molecular plane. See: (a) Stanger, A. Nucleus-Independent Chemical Shifts (NICS): Distance Dependence and Revised Criteria for Aromaticity and Antiaromaticity. *J. Org. Chem.* **2006**, *71*, 883−893. (b) Gershoni-Poranne, R.; Stanger, A. The NICS-*XY*-Scan: Identification of Local and Global Ring Currents in Multi-Ring Systems. *Chem. − Eur. J.* **2014**, *20*, 5673−5688. (c) Stanger, A. Reexamination of $NICS_{\pi,zz}$: Height Dependence, Off-Center Values, and Integration. *J. Phys. Chem. A* **2019**, *123*, 3922−3927.
(43) Kleinpeter and coworkers introduced three dimensional NICS maps − ICSS method. See: (a) Kleinpeter, E.; Klod, S.; Koch, A. Visualization of Through Space NMR Shieldings of Aromatic and Anti-aromatic Molecules and A Simple Means to Compare and Estimate Aromaticity. *J. Mol. Struct.: THEOCHEM* **2007**, *811*, 45−60. (b) Klod, S.; Kleinpeter, E. *Ab initio* Calculation of the Anisotropy Effect of Multiple Bonds and the Ring Current Effect of Arenes—Application in Conformational and Configurational Analysis. *J. Chem. Soc., Perkin Trans. 2* **2001**, 1893−1898.
(44) Scheer, H.; Katz, J. J. Nuclear Magnetic Resonance Spectroscopy of Porphyrins and Metalloporphyrins. In *Porphyrins and Metalloporphyrins*; Smith, K. M., Ed.; Elsevier: New York, 1975; Chapter 10, pp 399−524.
(45) The difference in the average vertical positions of the methylene units between **9-C*n*** and **13-C*n*** also affects their different $\Delta\delta$ values, although the degree of its contribution seems to be small.
(46) Shimizu, D.; Osuka, A. Porphyrinoids as a Platform of Stable Radicals. *Chem. Sci.* **2018**, *9*, 1408−1423.
(47) Krishnan, R.; Binkley, J. S.; Seeger, R.; Pople, J. A. Self-consistent Molecular Orbital Methods. XX. A Basis Set for Correlated Wave Functions. *J. Chem. Phys.* **1980**, *72*, 650−654.
(48) (a) Wachters, A. J. H. Gaussian Basis Set for Molecular Wavefunctions Containing Third-Row Atoms. *J. Chem. Phys.* **1970**, *52*, 1033−1036. (b) Hay, P. J. Gaussian Basis Sets for Molecular Calculations. The Representation of 3*d* Orbitals in Transition-Metal Atoms. *J. Chem. Phys.* **1977**, *66*, 4377−4384. (c) Raghavachari, K.; Trucks, G. W. Highly Correlated Systems. Excitation Energies of First Row Transition Metals Sc−Cu. *J. Chem. Phys.* **1989**, *91*, 1062−1065.
(49) (a) Becke, A. D. Density-Functional Thermochemistry. III. The Role of Exact Exchange. *J. Chem. Phys.* **1993**, *98*, 5648−5652. (b) Lee, C.; Yang, W.; Parr, R. G. Development of The Colle-Salvetti Correlation-Energy Formula into A Functional of The Electron Density. *Phys. Rev. B* **1988**, *37*, 785−789.
(50) (a) Hehre, W. J.; Ditchfield, R.; Pople, J. A. Self—Consistent Molecular Orbital Methods. XII. Further Extensions of Gaussian—Type Basis Sets for Use in Molecular Orbital Studies of Organic

https://dx.doi.org/10.1021/acs.joc.0c02433
J. Org. Chem. 2021, 86, 2283−2296

Molecules. *J. Chem. Phys.* **1972**, *56*, 2257−2261. (b) Hariharan, P. C.; Pople, J. A. The Influence of Polarization Functions on Molecular Orbital Hydrogenation Energies. *Theor. Chim. Acta* **1973**, *28*, 213−222. (c) Clark, T.; Chandrasekhar, J.; Spitznagel, G. W.; Schleyer, P. v. R. Efficient Diffuse Function-Augmented Basis Sets for Anion Calculations. III. The 3-21+G Basis Set for First-Row Elements, Li−F. *J. Comput. Chem.* **1983**, *4*, 294−301. (d) Rassolov, V. A.; Pople, J. A.; Ratner, M. A.; Windus, T. L. 6-31G* Basis Set for Atoms K Through Zn. *J. Chem. Phys.* **1998**, *109*, 1223−1229.

(51) Frisch, M. J.; Trucks, G. W.; Schlegel, H. B.; Scuseria, G. E.; Robb, M. A.; Cheeseman, J. R.; Scalmani, G.; Barone, V.; Petersson, G. A.; Nakatsuji, H.; Li, X.; Caricato, M.; Marenich, A. V.; Bloino, J.; Janesko, B. G.; Gomperts, R.; Mennucci, B.; Hratchian, H. P.; Ortiz, J. V.; Izmaylov, A. F.; Sonnenberg, J. L.; Williams-Young, D.; Ding, F.; Lipparini, F.; Egidi, F.; Goings, J.; Peng, B.; Petrone, A.; Henderson, T.; Ranasinghe, D.; Zakrzewski, V. G.; Gao, J.; Rega, N.; Zheng, G.; Liang, W.; Hada, M.; Ehara, M.; Toyota, K.; Fukuda, R.; Hasegawa, J.; Ishida, M.; Nakajima, T.; Honda, Y.; Kitao, O.; Nakai, H.; Vreven, T.; Throssell, K.; Montgomery, J. A., Jr.; Peralta, J. E.; Ogliaro, F.; Bearpark, M. J.; Heyd, J. J.; Brothers, E. N.; Kudin, K. N.; Staroverov, V. N.; Keith, T. A.; Kobayashi, R.; Normand, J.; Raghavachari, K.; Rendell, A. P.; Burant, J. C.; Iyengar, S. S.; Tomasi, J.; Cossi, M.; Millam, J. M.; Klene, M.; Adamo, C.; Cammi, R.; Ochterski, J. W.; Martin, R. L.; Morokuma, K.; Farkas, O.; Foresman, J. B.; Fox, D. J. *Gaussian 16*, Revision C.01; Gaussian, Inc.: Wallingford CT, 2019.

(52) Stoll, S.; Schweiger, A. EasySpin, A Comprehensive Software Package for Spectral Simulation and Analysis in EPR. *J. Magn. Reson.* **2006**, *178*, 42−55.

https://dx.doi.org/10.1021/acs.joc.0c02433
J. Org. Chem. 2021, 86, 2283−2296